Plasma Sources Sci. Technol. 28 (2019) 105005 (19pp)

https://doi.org/10.1088/1361-6595/ab30b7

A xenon collisional-radiative model applicable to electric propulsion devices: II. Kinetics of the 6*s*, 6*p*, and 5*d* states of atoms and ions in Hall thrusters

Xi-Ming Zhu^{1,4}, Yan-Fei Wang¹, Yang Wang^{1,4}, Da-Ren Yu¹, Oleg Zatsarinny², Klaus Bartschat², Tsanko Vaskov Tsankov³ and Uwe Czarnetzki³

E-mail: simon.ximing.zhu@outlook.com and yangwang0624@foxmail.com

Received 22 January 2019, revised 20 June 2019 Accepted for publication 5 July 2019 Published 7 October 2019



Abstract

Electric propulsion devices of using xenon propellant are nowadays widely adopted for the space missions. A collisional-radiative (CR) model of xenon needs to be developed to understand the kinetic mechanisms of the excited and energetic species in these devices and also to support their optical diagnostics. Previously, due to limitations in the fundamental cross section data, Xe CR models focused on the atomic species; the ionic species, which also play important roles for the thrusters, were not studied in detail. In our previous paper, a fully relativistic Dirac *B*-spline *R*-matrix method was applied to calculate the relevant cross sections for electron collisions with the Xe⁺ ion. Based on these data, a comprehensive CR model—with the kinetics of metastable and excited levels of both Xe and Xe⁺ included—could be built. The calculated density distributions of atomic and ionic levels are examined by optical measurements in Hall thrusters in all of the four typical regions (near-anode-, ionization-, acceleration-, and plume-region). The special kinetic behaviors of the excited species are analyzed, and a set of rate coefficient data used for the Xe CR model is also provided.

Supplementary material for this article is available online

Keywords: collisional-radiative model, electric propulsion, Hall thruster, xenon plasma

1

1. Introduction

In recent years, different kinds of electric propulsion (EP) systems were developed for aerospace missions, which became an important topic in the area of plasma source research [1–5]. Especially, Hall and ion thrusters of using xenon propellant have been used on many satellites [6, 7]. There are investigations on EP devices by fluid and particle-in-cell simulations [8–11] and diagnostic (probe, optical, and

laser) methods [12–17] and studies on new structures and materials for these devices [18, 19]. Xe collisional-radiative (CR) models for EP devices are also required to describe the kinetic behaviors of the excited species in numerical simulations as well as to predict the plasma emission spectra for diagnostic technique, e.g. by optical emission spectroscopy (OES) method.

Karabadzhak *et al* built a CR model for atomic levels of Xe [20], based on the optical cross sections measured by Chiu *et al* [21], to study the Hall thruster model D-55 in 2006. This model can predict the intensities of several emission lines in

¹ Harbin Institute of Technology, Harbin, Heilongjiang 150001, People's Republic of China

² Department of Physics and Astronomy, Drake University, Des Moines, IA 50311, United States of America

³ Institute for Plasma and Atomic Physics, Ruhr University Bochum, Bochum D-44780, Germany

⁴ Authors to whom any correspondence should be addressed.

the wavelength range of 789-980 nm and was used for an OES line-ratio method to measure the electron temperature (T_e) in the plume region of D-55. In 2009, Dressler et al improved the above CR model by utilizing the theoretical cross sections calculated by Zatsarinny and Bartschat using a semi-relativistic Breit-Pauli B-spline R-matrix (BSR) method and the data calculated by Srivastava and Sharma using a distorted-wave (DW) method [22]. This improved model was tested by the spectral data from D-55 as well as another Hall thruster, BHT-200, and it was then used to study the role of metastable states in these devices. Yang et al proposed another CR model with 173 atomic levels of Xe included for a Hall thruster in 2010 [23], based on cross sections obtained by the atomic code from the Los Alamos National Laboratory also with the DW method [24]. Their model was used for the optical diagnostics of an electron cyclotron resonant ion source in 2013 [25].

The previous models were mainly developed for investigating the Xe atomic levels and the atomic spectra from the plume region of thruster, and they cannot predict the intensities of ionic lines in the visible range, which play a dominant role when one uses CCD cameras for plume imaging [13]. In addition, the previous models adopt the assumption of an optically thin plasma, which can lead to inaccuracies for the near-anode- and ionization-regions of Hall thrusters.

In the present work, a CR model including both ionic and atomic excited levels is developed. It is based on the cross section and Einstein coefficient data calculated by a fully relativistic Dirac *B*-spline *R*-matrix (DBSR) method [26, 27]. To study the accuracy of this model, calculated atomic and ionic excited level density distributions are compared with those from optical measurements in the near-anode-, ionization-, acceleration-, and plume-region of Xe Hall thrusters. In addition, kinetic processes of the typical 6s, 6p, and 5d levels are analyzed in detail by using this model.

This paper is organized as follows. Section 2 describes the model while section 3 introduces the experiment. Section 4 compares the calculated and measured level density distributions, and investigates the dominant kinetic processes. Section 5 discusses the effect of the electron energy distribution. Conclusions are drawn in section 6. A supplemental database is available online at stacks.iop.org/PSST/28/105005/mmedia for the important rate coefficient data is given in the appendix.

2. CR model

This section introduces the energy levels (section 2.1), fundamental data (section 2.2), and kinetic processes (sections 2.3 and 2.4) of the CR model. The rate balance equations are given in section 2.5, from which the density distributions of both atomic and ionic excited levels can be obtained (and will be compared with the experiments in section 4).

Table 1. Xe(6p) levels in the present CR model.

Configuration	Term	J	E (eV)	NIST No	λ (nm)
$5p^5(^2P^{\circ}_{3/2}) 6p$	² [5/2]	3	9.721	8	881.9
$5p^5(^2P^{\circ}_{3/2}) 6p$	$^{2}[5/2]$	2	9.686	7	904.6, 992.3
$5p^{5}(^{2}P^{\circ}_{3/2}) 6p$	$^{2}[3/2]$	2	9.821	10	823.2, 895.2
$5p^5(^2P^{\circ}_{3/2}) 6p$	$^{2}[3/2]$	1	9.789	9	980.0
$5p^5(^2P^{\circ}_{3/2}) 6p$	$^{2}[1/2]$	1	9.580	6	840.9, 916.3
$5p^5(^2P^{\circ}_{3/2}) 6p$	$^{2}[1/2]$	0	9.933	13	828.0
$5p^5(^2P^{\circ}_{1/2}) 6p$	$^{2}[3/2]$	2	11.055	34	834.7
$5p^5(^2P^{\circ}_{1/2}) 6p$	$^{2}[3/2]$	1	10.958	24	820.6, 893.1
$5p^5(^2P^{\circ}_{1/2}) 6p$	$^{2}[1/2]$	1	11.069	36	764.2, 826.7
$5p^5(^2P^{\circ}_{1/2}) 6p$	$^{2}[1/2]$	0	11.141	38	788.7

2.1. Energy levels

This CR model focuses on the kinetics of the $5p^56s$, $5p^56p$, and $5p^55d$ levels of Xe and those of the $5p^46s$, $5p^46p$, and $5p^45d$ levels of Xe⁺. The atomic 7s, 7p, and 6d levels (called high-lying levels below) are also included, but the cross section data for the high-lying ionic levels are not available yet and these levels are not investigated here. Two ionic levels in $5s^25p^5$ group with J = 3/2 and J = 1/2 (J is quantum number for the total electronic angular momentum) are considered as separate levels, and the level $5s5p^6$ with a hole in the 5s subshell is included as well.

The $5p^56p$ and $5p^46p$ levels are the most important ones to study, because (i) their density distributions can be directly examined by the optical experiments and (ii) they are dominant for the OES diagnostics based on the CR model [20]. In addition, the 6s metastable levels of Xe, the 5d metastable levels of Xe⁺, and the 6s 'quasi-metastable' levels of Xe⁺ (i.e. the low-lying ionic levels with relatively long lifetimes) also play important roles, considering their contribution to the two-step excitation and ionization processes.

The following tables 1–6 provide information on the Xe(6p), $Xe^+(6p)$, Xe(6p), $Xe^+(6p)$, Xe(6p), $Xe^+(6p)$, Xe(5d), and $Xe^+(5d)$ levels, including the configuration, term, quantum number J, level energy E (relative to the ground state of Xe or Xe^+), vacuum wavelength λ of the experimentally observed strong lines (from the 6p levels). The column 'NIST No' provides the level number in order of increasing energy according to the NIST database [28].

2.2. Fundamental data

2.2.1. Excitation cross sections. Some of electron-impact cross sections can be experimentally determined, for example, by electron energy-loss spectroscopy (EELS) or an optical method. Buckman *et al* obtained an entire electron-impact excitation function for the Xe atom by the EELS method [29] while Allen *et al* measured the angle-differential cross sections for electron-impact excitation of Xe into the four $5p^56s$ levels [30]. By the optical method, Lin's group measured the electron-impact cross sections of Xe into the $5p^56p$ [31, 32] and $5p^57p$ levels [33] out of the ground state as well as the metastable levels. We note that the available experimental data in the literature cannot provide a full set of

Table 2. Xe⁺(6p) levels in the present CR model.

				NIST	
Configuration	Term	J	E (eV)	No	λ (nm)
$5p^4(^3P_2)6p$	² [3]°	7/2	14.098	31	484.4, 699.1
$5p^4(^3P_2)6p$	² [3]°	5/2	14.074	29	541.9, 553.1, 572.0
$5p^4(^3P_2)6p$	² [2]°	5/2	13.881	26	529.2, 605.1
$5p^4(^3P_2)6p$	² [2]°	3/2	13.860	25	533.9, 597.7, 609.8
$5p^4(^3P_2)6p$	² [1]°	3/2	14.479	35	460.3, 714.9
$5p^4(^3P_2)6p$	² [1]°	1/2	14.094	30	537.2, 566.8
$5p^4(^3P_1)6p$	² [2]°	5/2	15.264	41	492.1, 680.6
$5p^4(^3P_1)6p$	² [2]°	3/2	15.282	42	526.0, 577.6
$5p^4(^3P_1)6p$	² [1]°	3/2	15.410	44	575.1
$5p^4(^3P_1)6p$	² [1]°	1/2	15.445	46	754.8
$5p^4(^3P_1)6p$	² [0]°	1/2	15.024	39	543.9
$5p^4(^3P_0)6p$	² [1]°	3/2	15.080	40	488.4
$5p^4(^3P_0)6p$	² [1]°	1/2	14.930	37	519.1
$5p^4(^1D_2)6p$	² [3]°	7/2	16.126	52	487.7, 575.9, 659.5
$5p^4(^1D_2)6p$	² [3]°	5/2	15.978	49	627.1, 716.5
$5p^4(^1D_2)6p$	² [2]°	5/2	16.392	54	572.7
$5p^4(^1D_2)6p$	² [2]°	3/2	16.356	53	526.2
$5p^4(^1D_2)6p$	² [1]°	3/2	16.077	51	497.3, 597.1
$5p^4(^1D_2)6p$	² [1]°	1/2	16.458	56	504.5
$5p^4(^1S_0)6p$	² [1]°	3/2	18.497	105	
$5p^4(^1S_0)6p$	² [1]°	1/2	18.378	101	

Table 3. Xe(6s) levels in the present CR model.

Configuration	Term	J	E(eV)	NIST No
$\frac{5p^{5}(^{2}P^{\circ}_{3/2})6s}{5p^{5}(^{2}P^{\circ}_{3/2})6s}$	² [3/2]°	2	8.315	2
$5p^5(^2P^{\circ}_{3/2})6s$	$^{2}[3/2]^{\circ}$	1	8.437	3
$5p^{5}(^{2}P^{\circ}_{1/2})6s$	$^{2}[1/2]^{\circ}$	1	9.570	5
$5p^5(^2P^{\circ}_{1/2})6s$	$^{2}[1/2]^{\circ}$	0	9.447	4

Table 4. $Xe^+(6s)$ levels in the present CR model.

Configuration	Term	J	E(eV)	NIST No
$5p^4(^3P_2)6s$	² [2]	5/2	11.539	4
$5p^4(^3P_2)6s$	$^{2}[2]$	3/2	11.786	5
$5p^4(^3P_1)6s$	$^{2}[1]$	3/2	12.745	13
$5p^4(^3P_1)6s$	$^{2}[1]$	1/2	13.255	18
$5p^4(^3P_0)6s$	$^{2}[0]$	1/2	12.542	11
$5p^4(^1D_2)6s$	$^{2}[2]$	5/2	13.584	23
$5p^4(^1D_2)6s$	$^{2}[2]$	3/2	14.001	28
$5p^4(^1S_0)6s$	² [0]	1/2	16.025	50

cross section data for a comprehensive Xe CR model. To our knowledge, the excitation cross sections for the Xe⁺ ion in particular have not been measured; even for the atoms, the data for excitations out of the resonance states and many excited states are not available.

As seen in paper [26], DW and *R*-matrix (close-coupling) methods have been used for calculating *e*-Xe and *e*-Xe⁺ collision cross sections. The former is believed to be accurate for electrons of sufficiently high energy (tens to hundreds of eV), provided the target structure is described sufficiently well. At low incident energies, in particular below the

Table 5. Xe(5d) levels in the present CR model.

Configuration	Term	J	E (eV)	NIST No
$5p^5(^2P^{\circ}_{3/2})5d$	² [7/2]°	4	9.943	14
$5p^5(^2P^{\circ}_{3/2})5d$	$^{2}[7/2]^{\circ}$	3	10.039	16
$5p^5(^2P^{\circ}_{3/2})5d$	$^{2}[5/2]^{\circ}$	3	10.220	18
$5p^5(^2P^{\circ}_{3/2})5d$	$^{2}[5/2]^{\circ}$	2	10.158	17
$5p^5(^2P^{\circ}_{3/2})5d$	$^{2}[3/2]^{\circ}$	2	9.959	15
$5p^5(^2P^{\circ}_{3/2})5d$	$^{2}[3/2]^{\circ}$	1	10.401	19
$5p^5(^2P^{\circ}_{3/2})5d$	$^{2}[1/2]^{\circ}$	1	9.917	12
$5p^5(^2P^{\circ}_{3/2})5d$	$^{2}[1/2]^{\circ}$	0	9.890	11
$5p^5(^2P^{\circ}_{1/2})5d$	$^{2}[5/2]^{\circ}$	3	11.375	52
$5p^{5}(^{2}P^{\circ}_{1/2})5d$	$^{2}[5/2]^{\circ}$	2	11.302	50
$5p^5(^2P^{\circ}_{1/2})5d$	$^{2}[3/2]^{\circ}$	2	11.338	51
$5p^5(^2P^{\circ}_{1/2})5d$	$^{2}[3/2]^{\circ}$	1	11.607	85

Table 6. $Xe^+(5d)$ levels in the present CR model.

Configuration	Term	J	<i>E</i> (eV)	NIST No.
$5p^4(^3P_2)5d$	² [4]	9/2	12.325	10
$5p^4(^3P_2)5d$	$^{2}[4]$	7/2	12.589	12
$5p^4(^3P_2)5d$	$^{2}[3]$	7/2	11.833	7
$5p^4(^3P_2)5d$	$^{2}[3]$	5/2	13.201	17
$5p^4(^3P_2)5d$	$^{2}[2]$	5/2	11.828	6
$5p^4(^3P_2)5d$	$^{2}[2]$	3/2	11.907	8
$5p^4(^3P_2)5d$	$^{2}[1]$	3/2	13.057	15
$5p^4(^3P_2)5d$	$^{2}[1]$	1/2	12.009	9
$5p^4(^3P_2)5d$	$^{2}[0]$	1/2	13.136	16
$5p^4(^3P_1)5d$	$^{2}[3]$	7/2	13.443	22
$5p^4(^3P_1)5d$	$^{2}[3]$	5/2	14.227	32
$5p^4(^3P_1)5d$	$^{2}[2]$	5/2	13.974	27
$5p^4(^3P_1)5d$	$^{2}[2]$	3/2	13.803	24
$5p^4(^3P_1)5d$	$^{2}[1]$	3/2	13.379	20
$5p^4(^3P_1)5d$	$^{2}[1]$	1/2	12.925	14
$5p^4(^3P_0)5d$	$^{2}[2]$	5/2	13.391	21
$5p^4(^3P_0)5d$	$^{2}[2]$	3/2	13.314	19
$5p^4(^{1}D_2)5d$	² [4]	9/2	14.246	33
$5p^4(^1D_2)5d$	$^{2}[4]$	7/2	14.248	34
$5p^4(^1D_2)5d$	$^{2}[3]$	7/2	14.984	38
$5p^4(^1D_2)5d$	² [3]	5/2	14.765	36
$5p^4(^{1}D_2)5d$	² [2]	5/2	15.412	45
$5p^4(^1D_2)5d$	$^{2}[2]$	3/2	15.811	48
$5p^4(^1D_2)5d$	$^{2}[1]$	3/2	15.383	43
$5p^4(^1D_2)5d$	$^{2}[1]$	1/2	15.747	47
$5p^4(^{1}D_2)5d$	$^{2}[0]$	1/2	16.745	58
$5p^4(^1S_0)5d$	² [2]	5/2	16.933	64
$5p^4(^1S_0)5d$	² [2]	3/2	17.118	66

ionization threshold, close-coupling is the method of choice [34]. Attempts to extend close-coupling to higher energies include the convergent close-coupling (CCC approach) [35] and the *R*-matrix with pseudo-states (RMPS) method [36, 37]. Only for the latter, general computer codes exist [38–41] that can handle complex targets. Calculations of Xe excitation cross sections by the DW approach can be found in [42–44] and those by a semi-relativistic Breit–Pauli *B*-spline *R*-matrix method in [27]. In the present work we use the cross sections calculated by a fully relativistic Dirac *B*-spline *R*-matrix (DBSR) method for electron-impact excitations between Xe

states [27] and those between Xe⁺ states [26]. A fully relativistic approach is necessary for Xe⁺ because of significant relativistic effects.

The electron-impact ionization-excitation out of the atomic ground state is important in the production of ionic 6p levels at high electron energy, and the ion-impact excitation and ionization-excitation processes play a role of producing atomic and ionic 6p levels in the acceleration- and plume-region. Apparent cross sections for these processes (from the atomic ground state to the 6p levels) can be obtained from the emission cross sections in [21, 45] and adopted in this model.

The ns and nd levels of Xe⁺ are also produced by the above processes; however, their cross sections are not measured. Note that some of the high levels in the ns or nd groups mainly decay to certain 6p levels; their contribution to these 6p levels, due to cascades following the above excitation processes, is already accounted for in the 6p apparent cross sections. Therefore, we do not consider the above processes for these ns or nd levels. This might lead to inaccuracies in their densities but keeps the results for 6p accurate. On the other hand, cascades from the 6p levels can be the dominant source for some of the low levels in the ns or nd groups; the above excitations are negligible in comparison. As for the other ns and nd levels, their excitations are considered separately in the model with the cross sections roughly estimated from that of the 6p level nearest to them. The accuracy of the 6p densities is not significantly influenced by this approximation, since there is no efficient coupling in kinetics between this kind of levels and the 6p levels.

2.2.2. Ionization cross sections. Reliable measurements of the ground-state ionization cross sections for Xe and Xe⁺ can be obtained from the literature, e.g. [46, 47], while the data for ionization of excited levels have not been measured. In principle, these data can be calculated by the DBSR method, but with a large-scale model of hundreds of target states and a large amount of computational resources. Since the ionization processes from excited levels are much less important to the rate balance of these species than their excitation processes (see section 4 below), we use the semi-empirical Deutsch-Märk formalism [48] for an estimate.

2.2.3. Charge exchange. Charge exchange (CEX) is another important process, for which experimental cross sections are available in the literature [49–51]. For the thrusters considered in the present work, a mean free path $>200 \, \mathrm{mm}$ is estimated from the gas density and the charge transfer cross sections, this being much larger than the characteristic length of the discharge channel of $\sim 10 \, \mathrm{mm}$. As a result, the CEX process is not significant in this channel. However, when investigating the plume region with a length of $\sim 1 \, \mathrm{m}$ or longer, CEX plays an important role in reducing the number of high-energy ions.

2.2.4. Einstein coefficients and diffusion coefficients. There exist reports of measurements of Einstein coefficients for

atomic and ionic transitions in Xe [52–54]. Calculated data can also be found [26, 27, 55]. Most of these theoretical and experimental data are in agreement with each other. For consistency we use the Einstein coefficients calculated by the DBSR method in [26, 27].

The diffusion-controlled wall deactivation is an important depopulation mechanism for the metastable atoms in the discharge channel of thrusters. Diffusion coefficients, as well as the two- or three-body collisional quenching coefficients, have been fully investigated e.g. in [56, 57]. From these data one can calculate the diffusion loss rate as well as estimate the atom-atom collisional quenching rate, and find the latter process is ignorable under the condition in this work.

2.3. Important kinetic processes

Among many types of kinetic processes in a rare-gas discharge [58], only some are important to the kinetics of the 6s, 6p, and 5d levels for the EP devices e.g. Hall thrusters. The processes excluded from the list of 'important processes' are labeled 'other processes' and discussed in the next section.

The important kinetic processes include: (i) electronimpact excitation and de-excitation,

$$e + Xe \leftrightarrow e + Xe^*,$$
 (1)

$$e + Xe^+ \leftrightarrow e + Xe^{+*},$$
 (2)

$$e + Xe^* \leftrightarrow e + Xe^{**},$$
 (3)

$$e + Xe^{+*} \leftrightarrow e + Xe^{+**},$$
 (4)

where e denotes an electron, Xe and Xe⁺ xenon atoms and ions in their ground-state, Xe^{*} and Xe^{+*} xenon atoms and ions in low-lying excited states, and Xe^{**} and Xe^{+**} excited atoms and ions in higher Rydberg levels (the excitation cross sections are calculated by the DBSR method and the deexcitation cross sections are given by the Klein–Rosseland formula [59] based on these data); (ii) electron-impact ionization

$$e + Xe/Xe^* \rightarrow 2e + Xe^+,$$
 (5)

$$e + Xe^{+}/Xe^{+*} \rightarrow 2e + Xe^{2+},$$
 (6)

where Xe^{2+} denotes doubly-ionized xenon ions; (iii) electron-impact ionization-excitation

$$e + Xe \rightarrow 2e + Xe^{+*}; \tag{7}$$

(iv) ion-impact excitation and ionization-excitation

$$Xe^{+h} + Xe \rightarrow Xe^* + product,$$
 (8)

$$Xe^{+h} + Xe \rightarrow Xe^{+*} + product,$$
 (9)

where Xe^{+h} means high-energy ions; (v) spontaneous radiation

$$Xe^*/Xe^{**} \to Xe/Xe^* + h\nu,$$
 (10)

$$Xe^{+*}/Xe^{+**} \to Xe^{+}/Xe^{+*} + h\nu,$$
 (11)

where hv denotes a photon; (vi) self-absorption (radiation trapping)

$$Xe/Xe^* + h\nu \to Xe^*/Xe^{**},$$
 (12)

$$Xe^{+}/Xe^{+*} + h\nu \rightarrow Xe^{+*}/Xe^{+**};$$
 (13)

(vii) charge exchange

$$Xe^{+h}/Xe^{+} + Xe \rightarrow Xe^{h}/Xe + Xe^{+},$$
 (14)

where Xe^h means high energy atoms; (viii) diffusion-controlled wall deactivation of the atomic metastables (in the discharge channel)

$$Xe^m \xrightarrow{\text{wall}} Xe,$$
 (15)

where Xe^m refers to the metastable levels of Xe. This list of processes covers the important kinetic mechanisms found in the previous EP modelling research reported, for example, in [20].

2.4. Other processes

Here we introduce some other processes and explain the reasons why they are not included in the model. Firstly, the electron-ion recombination process is ignored because its rate decays fast with increasing electron energy [58]. In a mean electron energy range \sim 5–20 eV of the EP devices, the recombination rate is smaller than the excitation rate by several orders of magnitude. Secondly, the Penning ionization process is found to be important only for high-pressure, weakly-ionized plasmas, e.g. at pressures >10 3 Pa and an ionization ratio <10 $^{-5}$ [58]. Processes involved with excimer (Xe₂*) and molecular ion (Xe₂+) play significant roles at even higher pressures, e.g. 10^4 Pa. Considering the neutral gas pressure in the thruster here is <1 Pa (section 3), the above processes can be ignored.

In principle, one should investigate the transport-controlled surface recombination for the ions in the metastable levels as a loss channel like the role of process (15) above. However, we find this process to be not important here. Notice that, for both the ionic metastable and quasi-metastable levels, e.g. $5p^45d$ $^{2}[3]^{\circ}_{7/2}$ and $5p^{4}6s^{2}[2]^{\circ}_{5/2}$, there are strong excitation channels to the 6p group, which can decay to other ns or nd levels and lead to an effective loss for the metastable and quasi-metastable levels. This is quite different from the phenomenon found in the rate balance of atomic metastable levels, e.g. $5p^56s^2[3/2]_2$, for which strong excitations to the 6p levels cannot lead to a fast loss since most of these 6p levels decay to level $5p^56s^2[3/2]_2$ in return. This can be understood from the different energy structures; the atomic 6s, 6p, and 5d groups are separated in energy, but the ionic 6s, 6p, and 5d groups are mixed. As a result, the ionic 6p levels have more radiative decay channels. To confirm this analysis, we estimated the loss frequency by this surface recombination of ionic levels using a particle-in-cell code [60] and found its contribution to be at most \sim 5% for the metastable levels and always <0.5% for the excited levels compared with other mechanisms.

As seen from equation (14), high-energy atoms can be produced by the CEX process. These atoms might play a role in the excitation process in the far-field plume region. The atom-impact excitation mechanism was studied in [61] in a high-voltage sheath of a glow discharge. Using the expression given in [61], we estimate the high-energy atom excitation cross section to be smaller than that of high-energy ion excitation cross section by about one order of magnitude at 500 eV. Hence we ignore the atom-impact excitation process, considering that (i) the flux of high-energy atoms cannot be

much larger than that of high-energy ions for the present thruster and (ii) the maximum contribution of the ion-impact excitation is only \sim 5%, as shown in section 4.

2.5. Rate balance equation

Considering all the important processes in section 2.3, the rate balance equation for the atomic and ionic excited levels (in a steady state) can be written as:

$$\sum_{y \neq x} R_{y \to x}^{\text{col}} + \sum_{y > x} R_{y \to x}^{\text{rad}} + \sum_{y < x} R_{y \to x}^{\text{abs}} = \sum_{y \neq x} R_{x \to y}^{\text{col}} + \sum_{y < x} R_{x \to y}^{\text{rad}} + \sum_{y > x} R_{x \to y}^{\text{abs}} + R_{x}^{d/t}.$$
(16)

Here R means reaction rate; 'col', 'rad', and 'abs' refer to collision (excitation, ionization, and ionization-excitation), radiation, and absorption processes, respectively. $R^{d/t}$ is the loss rate due to diffusion or transport. The subscript y refers to a level different from the excited level x, including the atomic and ionic ground states; y < x means level y is lower than level x in energy.

2.5.1. Collision terms. The collision terms in the above equations can be expressed as:

$$R_{y \to x}^{\text{col},e} = n_e \cdot n_y \cdot Q_{y \to x}^e$$
 and $R_{y \to x}^{\text{col},i} = n_i \cdot n_y \cdot Q_{y \to x}^i$. (17)

Here n_e and n_i are the electron and ion densities; the superscripts e and i denote the electron- and ion-impact processes. The electron-impact rate coefficient is calculated as:

$$Q_{y\to x}^e = \int_{E_0}^{\infty} \sigma_{y\to x}^e(E_e) \cdot \sqrt{\frac{2E_e}{m_e}} \cdot g_e(E_e) \cdot dE_e.$$
 (18)

Here σ^e is the electron-impact cross section for excitation, ionization, and ionization-excitation; E_e and m_e are the electron energy and mass; E_0 is the threshold energy for reaction; g_e is the electron energy distribution function (EEDF). In previous CR models Maxwellian EEDFs are often assumed for low-pressure discharges with relatively high electron densities [62, 63] and also for the plume region of Hall thrusters [22, 23], which can be confirmed by Langmuir probe measurements [64, 65] and simulations [66]. We also make this assumption for the plume region. As for the regions inside the discharge channel, however, special non-Maxwellian EEDF forms, e.g. the 'Bugrova distribution' [67, 68], are found for some widely-studied Hall thrusters such as the SPT series [69]. The Bugrova distribution is expressed as:

$$g_e(E_e) = \frac{15}{4} u^{-5/2} E_e^{-1/2} (u - E_e) \text{ with } 0 \leqslant E_e \leqslant u$$

and $\overline{E_e} = \frac{3}{7} u = \frac{3}{2} T_e.$ (19)

Here T_e is an 'effective electron temperature' defined for the Bugrova distribution through the mean electron energy. The physical mechanisms for the above EEDF form have been explained by Bugrova and co-authors [67, 68]. Specifically, the electron-wall interaction plays an important role in Hall thrusters. High-energy electrons can overcome the potential barrier of the wall sheath, lose their energy when reaching the wall, and return to the plasma bulk with low energy. This causes de-population of high-energy electrons and the production of low-energy electrons. As a result, the Maxwellian distribution formed outside the channel is changed into a Bugrova distribution inside the channel. In this work, we investigate the near-anode-, ionization-, and acceleration-region of a Hall thruster HET-P70 of our group. It is developed based on an SPT-70 thruster and has similar dynamic characteristics. So we assume a Bugrova EEDF and further analyze it in section 5.

The ion-impact rate coefficient in equation (17) should be calculated by:

$$Q_{y\to x}^i = \int_{E_0}^{\infty} \sigma_{y\to x}^i(E_i) \cdot \sqrt{\frac{2E_i}{m_i}} \cdot g_i(E_i) \cdot dE_i, \qquad (20)$$

where σ^i , E_i , m_i , and g_i denote the ion-impact cross section, ion energy, ion mass, and ion energy distribution function (IEDF), respectively. The ion-impact process is actually only important for the plume region, where we use a retarding potential analyzer (RPA) to measure the EDF as done in [70]. If an RPA is unavailable, one could use a simplified form:

$$Q_{y\to x}^{i} = \xi(E_{V}) \cdot \sigma_{y\to x}^{i}(E_{V}) \cdot \sqrt{\frac{2E_{V}}{m_{i}}} \text{ with } \xi(E_{V})$$
$$= \exp(-\sigma_{\text{CEX}}(E_{V}) \cdot n_{a} \cdot d). \tag{21}$$

Here E_V is the ion energy according to the applied voltage and the factor ξ accounts for the loss of high-energy ions by charge exchange (σ_{CEX} is the charge exchange cross section, n_a is the atom density, and d is the distance from the channel exit). This form can also be used for the acceleration region by changing the value E_V according to the electric potential drop and using $\xi \approx 1$ (the length of acceleration region is much shorter than the mean free path of ions in this region). Equation (21) provides a zero-order estimate of the IEDF. It is acceptable when the contribution of the ion-impact process is small (e.g. $\sim 5\%$ in this work). A more accurate calculation of IEDF can be obtained by models like those developed in [71, 72].

2.5.2. Radiation and absorption terms. The radiation and absorption terms in the rate equation (16) can be expressed as:

$$R_{y\to x}^{\text{rad}} - R_{x\to y}^{\text{abs}} = \Gamma_{y\to x}(n_x) \cdot A_{y\to x} \cdot n_y.$$
 (22)

Here y is the upper level and x is the lower level; A is the Einstein coefficient for spontaneous radiation and Γ is the escape factor. Equation (22) is actually a simplified expression for describing the radiation trapping phenomenon in a plasma medium. A detailed investigation of this topic was performed in our previous work [73], and the escape factor is

given by:

$$\Gamma(\tau) = \frac{2 - \exp(-c_1 \cdot \tau)}{1 + (c_2 \cdot \tau)^k}.$$
 (23)

Here τ is the optical depth of plasma calculated by equation (16) in [73] from the lower level density n_x and the plasma radius r. The coefficients c_1 , c_2 , and k can be found in [73].

2.5.3. Diffusion and transport terms. As mentioned in section 2.3, the diffusion-controlled wall deactivation of the Xe(6s) metastables should be included, whose rate is calculated by [74]:

$$R_x^{d/t} = K_x \cdot n_x \text{ and } K_x^{-1} = \left(D_x \cdot \frac{\chi_{01}^2}{r^2}\right)^{-1} + \left(\frac{v_0}{r}\right)^{-1}.$$
 (24)

Here D_x is the diffusion coefficient of species x, r the radius of plasma, v_0 the mean speed of atoms, and χ_{01} 2.405. The cross section of discharge channel is a ring, and we use approximation $r = (r_{\text{out}} - r_{\text{in}})/2$ in equation (24). Here r_{out} and r_{in} are the radii of the outer and inner walls, respectively. In the far-field plume region (e.g. 600 mm from exit), the plasma expands to the whole discharge chamber (radius 1 m here) with a bright region (radius of the order of magnitude of 0.1 m) in the axial center. In this case, the density gradient of excited species is much smaller than in the channel, and the self-absorption effect and diffusion loss are weak and ignorable for the metastable and 6p levels⁵.

As explained in section 2.4, the transport loss of ionic metastable and excited levels is much less important than the electron-impact depopulation; however, for two lowest states, $5s^25p^5$ $^2P^{\circ}_{3/2}$ and $5s^25p^5$ $^2P^{\circ}_{1/2}$ of Xe⁺, the transport term in equation (16) is not negligible. In this case, we write:

$$R_p^{d/t} = C_p \cdot n_p \text{ and } R_q^{d/t} = C_q \cdot n_q.$$
 (25)

Here p and q refer to the levels $5s^25p^5$ $^2\mathrm{P^o}_{3/2}$ and $5s^25p^5$ $^2\mathrm{P^o}_{1/2}$, respectively; n and C are their densities and the loss frequencies due to transport. We introduce two approximations:

$$C_p \approx C_q \text{ and } n_p + n_q \approx n_e,$$
 (26)

where n_e is electron density (quasi-neutrality). From equations (16), (25) and (26), n_p and n_q can be obtained.

⁵ Here an effective plasma radius is still needed in the model, mainly to give the escape factor of the resonance radiation lines, which is roughly estimated by $r = r_{\rm out} + \tan\theta \cdot d$ (θ is the plume divergence angle [75] and d the distance from the channel exit). Inaccuracy caused by this assumption is acceptable when the excitation processes from 6s and 5d resonance levels are not important for the 6p levels, as found by the CR model for the plume region in our thruster.

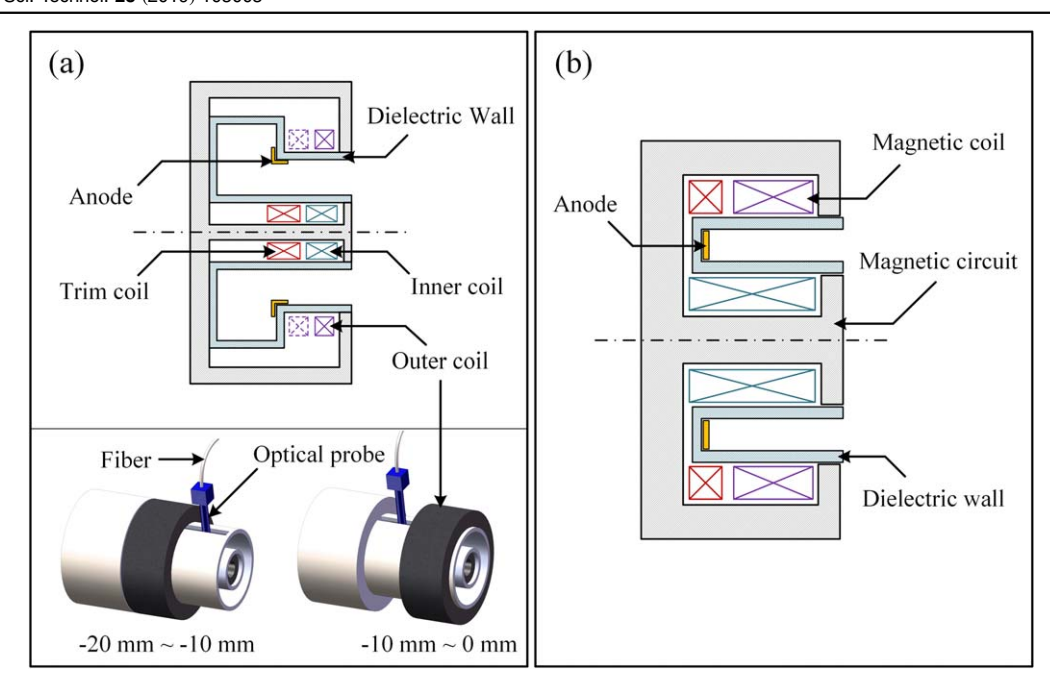


Figure 1. Diagrams of the Hall thrusters HET-P70 (a) and HET-140 (b). The small stereograms in (a) show how to observe the plasma inside the channel (introduced in detail in section 3.2).

Table 7. Plasma parameters for specific positions in two Hall thrusters. Positive position means outside of the channel exit and negative for inside; the distance from anode to exit is 20 mm for HET-P70. T_e , n_e , n_g , E_i , and r refer to the electron temperature (effective value for the Bugrova distribution), electron density, neutral gas density, ion energy, and plasma radius, respectively.

Device	Position (mm)	T_e (eV)	$n_e (10^{11} \text{ cm}^{-3})$	$n_g (10^{12} \text{ cm}^{-3})$	E_i (eV)	r (mm)	EEDF
P70	-13	8	1	20	_	7	Bugrova
P70	-8	12	2	6		7	Bugrova
P70	-3	18	6	4	120	7	Bugrova
P140	600	5	1.5	1.5	500	230	Maxwellian

3. Experiment

3.1. Hall thruster

Experiments in the present work are performed on two models of Hall thrusters using Xe as working gas. The first model HET-P70 (power \sim 1 kW, channel diameter 70 mm) is an Aton-type Hall thruster, which was developed based on the SPT series with the device structure and magnetic field design improved. The typical plume half divergence angle is \sim 20°. To enhance the focusing effect, another model HET-P140 (power \sim 5 kW, channel diameter 140 mm) was developed more recently, for which the plume half divergence angle is <15°. Figure 1 shows the schematic diagrams of these thrusters. Both consist of a discharge channel, anode, magnetic coils, magnetic circuit, and hollow cathode (omitted in figure for clarity). HET-P70 is operated at a voltage of 300 V and gas flow rate of 35 sccm (99.999% Xe), while HET-P140 is operated at 500 V and 100 sccm.

HET-P70 is used to examine the prediction of the CR model in the near-anode-, ionization-, and acceleration-region, considering that its physical characteristics are essentially similar to the SPT series and were fully studied

during the past decade [76–81]. For example, the electron energy distribution in the channel of HET-P70 was found to generally obey the Bugrova distribution [81], the plasma parameters, including the electron temperature or mean electron energy, electron density, gas density, gas temperature, and pressure were known from a serial of experiment and simulation works [60, 76, 77, 81–84], and the method of changing the ionization distribution in the discharge channel was also fully studied [81]. In addition, benchmark validation of the simulation code for HET-P70 was done like that in [85] by comparing the performance parameters (discharge current, thrust, and anode efficiency) from simulation and experiment. Major plasma parameters of HET-P70 in the near-anode, ionization-, and acceleration-region are given in table 7.

In addition to the above regions, the far-field plume region—at a distance much longer than the mean free path of the ions—is also concerned for EP research due to the background gas effect. However, the ionic emission lines in the far-field plume region of HET-P70 (e.g. at distances >500 mm) are too weak in the optical measurement due to relatively large plume divergence angle and small discharge current. We use the HET-P140 thruster instead to examine the model, considering that the plasma properties in its plume

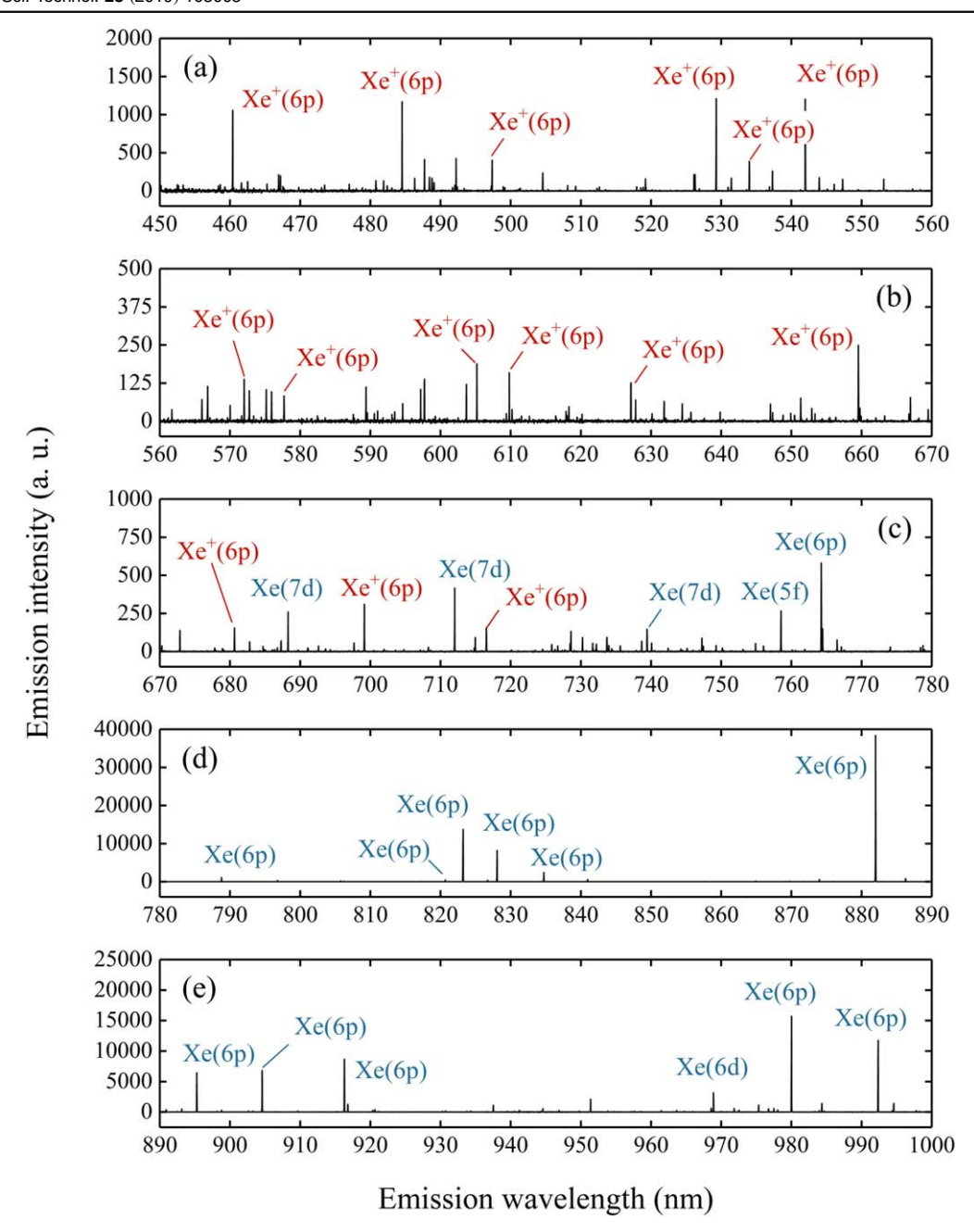


Figure 2. Typical emission spectrum in the channel (position -5 mm) of HET-P70.

region can be studied by using a Langmuir probe (electron density and EEDF), a Faraday probe (ion current), and an RPA (IEDF) like in [70, 86]. The gas temperature in the plume region is obtained by simulations considering the CEX effect [81], and then the gas density can be calculated from the measured gauge pressure.

In table 7 four specific positions are selected for (i) relatively good signals in the optical measurements and (ii) typically different plasma properties. The region with too weak ionic lines, the transition region between ionization and acceleration regions, and the near-field plume region without specific kinetic processes are excluded. In section 3.2 we explain this selection in more detail by showing the spatial intensity distribution of the atomic and ionic emission lines.

3.2. Optical measurement

In order to measure the emission spectra in the far-field plume region (at 600 mm from the exit), an optical fiber is fixed along the radial direction of the HET-P140 channel and at a distance of 500 mm from its axis (i.e. out of the plume region with radius of 230 mm). A Horiba FHR-1000 CCD spectrometer is used to obtain the spectra in the wavelength range of 300–1000 nm. With a slit width of 20 μ m in the experiment, the spectral resolution is \sim 0.05 nm. The entire optical system is calibrated by a tungsten ribbon lamp for a relative spectral response.

A specific structure is designed to measure the emission spectra inside the discharge channel of HET-P70 [77]. As

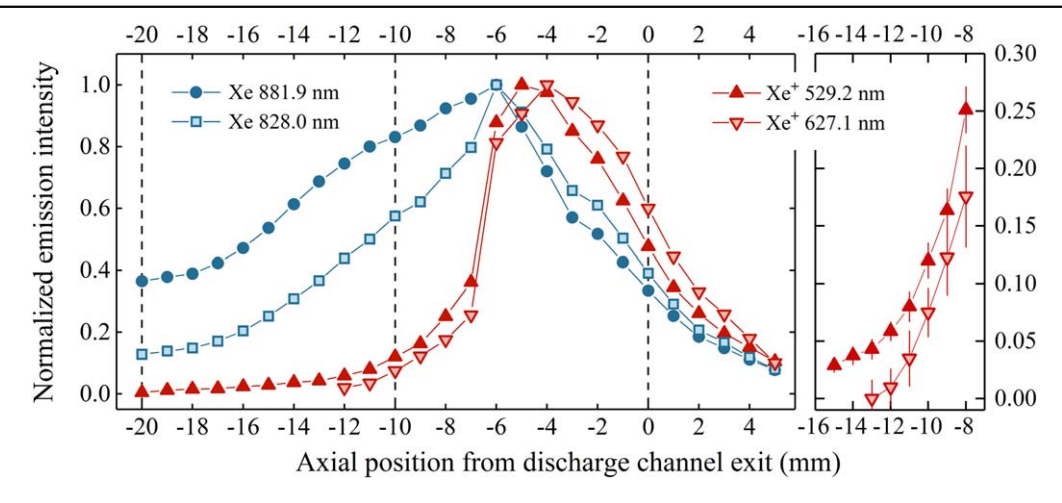


Figure 3. Emission intensities of four lines in HET-P70. For clarity the uncertainties of weak lines are separately shown on the right.

seen in figure 1(a), the outer coils can be moved between two positions and an optical probe made of ceramic (length 40 mm, outer diameter 3 mm, and inner diameter 2 mm) is inserted into the narrow slit (width 4 mm) on the outer wall. The emission in the near-anode-, ionization-, and acceleration-region is thus observed by the fiber connected to this optical probe.

Before studying the inside plasma, one needs to make sure that (i) the slit is sufficiently narrow so that the state of the working gas is not significantly affected and (ii) the magnetic field in and around the channel is not significantly affected either by moving the coils. Therefore, before carrying out the optical measurements, we compare the performances of two HET-P70 thrusters with and without the slit as well as the performances when the outer coils are at different positions. We found that all the major parameters are unchanged in these cases, because (i) the slit width is much smaller than the channel size and (ii) the magnetic field shape is determined by the magnetic circuit.

Figure 2 shows a typical spectrum measured in the channel of HET-P70 (at -5 mm). The upper levels of relatively strong lines are indicated. In general, the $Xe^+(6p)$ lines are dominant in the range of 450–700 nm, i.e. the visible range often concerned for a camera imaging research [13, 87]; most of the Xe(6p) lines are in the range of 800–1000 nm.

Actually, from the spatially resolved emission line intensities, one could also investigate the change of plasma state in the different regions, in addition to simulation and probe methods used before [76, 83, 84]. Figure 3 shows the normalized emission intensities of four typical lines from the Xe(6p) and $Xe^+(6p)$ groups, from -20 mm (anode edge) to 5 mm (outside of the channel exit). The intensity profiles of these lines are significantly different.

For example, the ionic lines are very weak in the region from -20 to -10 mm; lines from relatively high levels (e.g. 627.1 nm) are difficult to be measured at <-12 mm. This is due to it being in the near-anode region with a low ionization ratio. From about -10 to -5 mm, the intensity of the ionic lines increases fast; especially, a sharp increase is found around -7 mm. This is the ionization region. After that, the

ionic line intensity reduces due to the acceleration process (higher speed and lower density). The atomic density decreases in the ionization region, while the electron temperature peaks in the transition zone between the ionization and acceleration regions [77]. As a result, a peak of atomic line intensities is observed near -6 mm.

4. Results

There are two main topics to be dealt with in this section. Firstly, calculated and measured level density distributions are compared to examine the accuracy of the model. The former results are obtained by solving the rate equations in section 2 (using parameters in table 7), and the latter are given by dividing the measured line intensities by the corresponding Einstein coefficients. For almost all upper levels we can find a line with the lower level not being metastable and thus not affected by the radiation trapping process. The only exception is $(^2P^{\circ}_{3/2})$ $^2[5/2]_3$ of Xe(6p), for which we consider the escape factor from the model when obtaining its level density. After the comparison of level density distribution, the detailed kinetic processes of 6p, 6s, and 5d levels are investigated.

4.1. Experimental and modelling 6p level densities

Figures 4–7 show the calculated and measured densities of ten Xe(6p) levels and nineteen $Xe^+(6p)$ levels for the positions -13, -8, and -3 mm of thruster HET-P70 and that at position 600 mm of HET-P140. The total density is normalized to unity for comparison, considering the emission lineratios in experiment give relative species densities. These levels are divided into several groups according to the cores $(^2P_{3/2}$ and $^2P_{1/2}$ for Xe and 3P_2 , 3P_1 , 3P_0 , and 1D_2 for Xe⁺).

The error bars in figure 4 reflect the uncertainty in experimental density (discussed in detail later). The experimental densities of high $\mathrm{Xe}^+(6p)$ levels between ${}^3\mathrm{P}_2$ ${}^2[1]^\circ_{3/2}$ and ${}^1\mathrm{D}_2$ ${}^2[1]^\circ_{1/2}$ are not given here, since the signal of their emission lines is even lower than the noise at this position (see line 627.1 nm in figure 3). As for the levels $({}^1\mathrm{S}_0)$ ${}^2[1]^\circ_{3/2}$

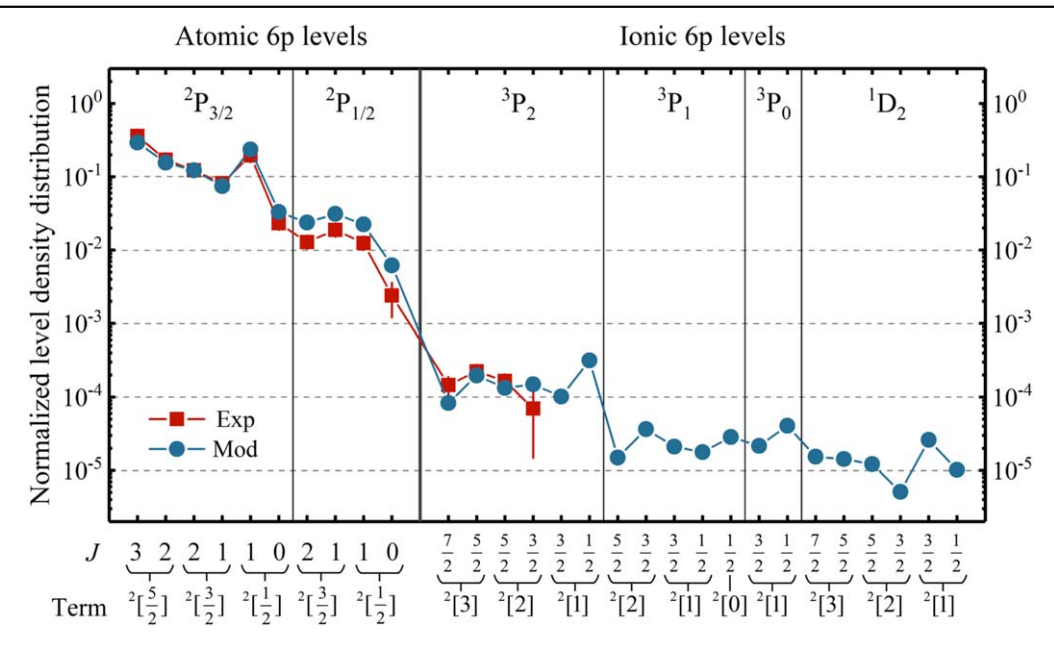


Figure 4. Normalized density of Xe(6p) and $Xe^+(6p)$ levels at -13 mm of thruster P70 (near-anode region). 'Exp' and 'Mod' denote the results by optical measurement and CR model, respectively.

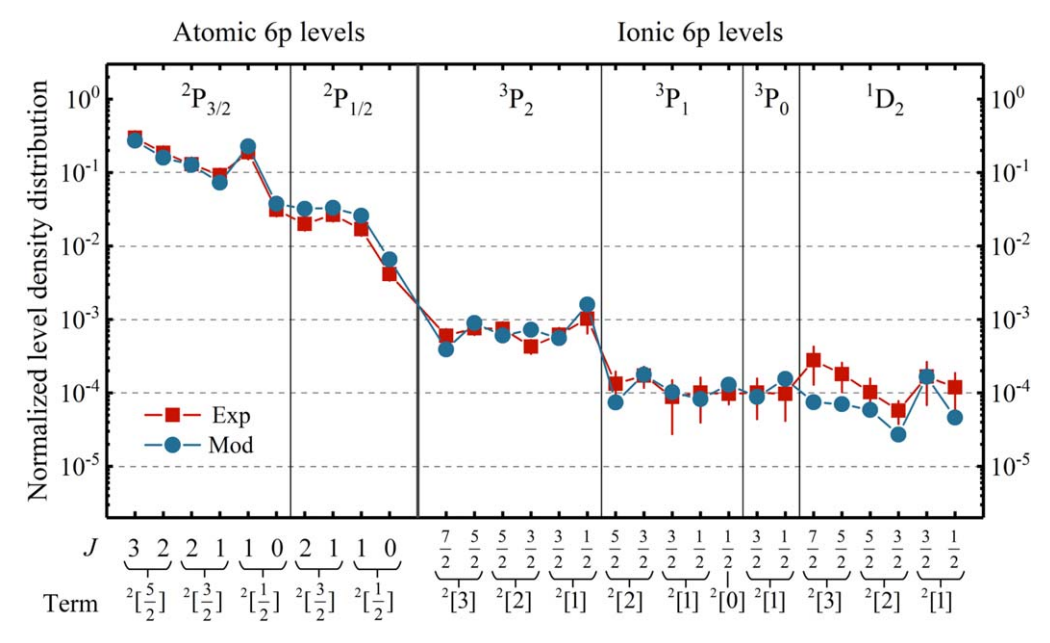


Figure 5. Normalized density of 6p levels in the ionization region (-8 mm).

and $(^{1}S_{0})^{2}[1]^{\circ}_{1/2}$ of $Xe^{+}(6p)$, their emission lines are not observed in this work.

In general, we find that the modelling and experimental results, especially for the $^2P_{3/2}$ group emitting strong lines, are in agreement here. The relative densities of the ionic 6p levels are only $\sim 10^{-4} - 10^{-5}$. The position of figure 4 (-13 mm) is already near to the edge between near-anode- and ionization-region; for a position nearer to the anode, the ionic lines are even weaker.

In the ionization region the relative density of $Xe^+(6p)$ is increased; in figure 5 (position -8 mm) it is $\sim 10^{-3}-10^{-4}$, higher than that in the near-anode region by a factor $\sim 5-10$. Actually, in table 7 the plasma density at -8 mm is higher

than that at -13 mm only by a factor of 2. However, the production rate of $Xe^+(6p)$ is roughly proportional to the square of the plasma density and also increases significantly with the electron temperature.

Figure 6 shows the level density for the position -3 mm, being in the acceleration region and near the position of ionic line intensity peak in figure 3. We see that the shape of the curve in figure 6 becomes different from the above figures; specifically it changes from a ladder-like shape to a relatively flat curve. The density of the ionic 3P_2 group is even close to that of the atomic $^2P_{1/2}$ group. This is a result of large increases in both the electron temperature and density.

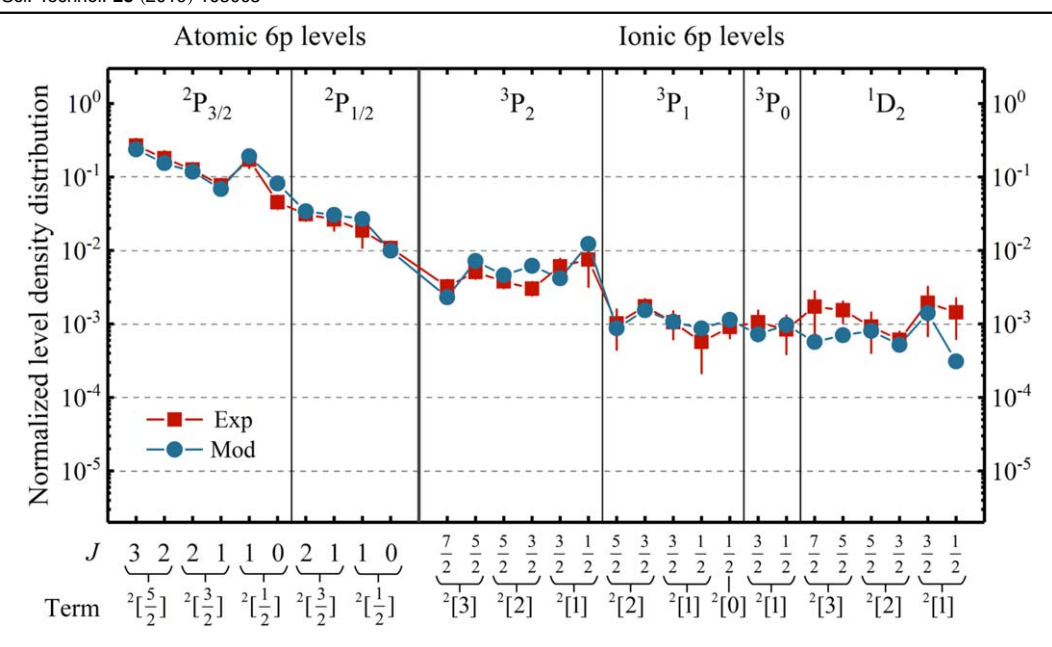


Figure 6. Normalized density of 6p levels in the acceleration region (-3 mm).

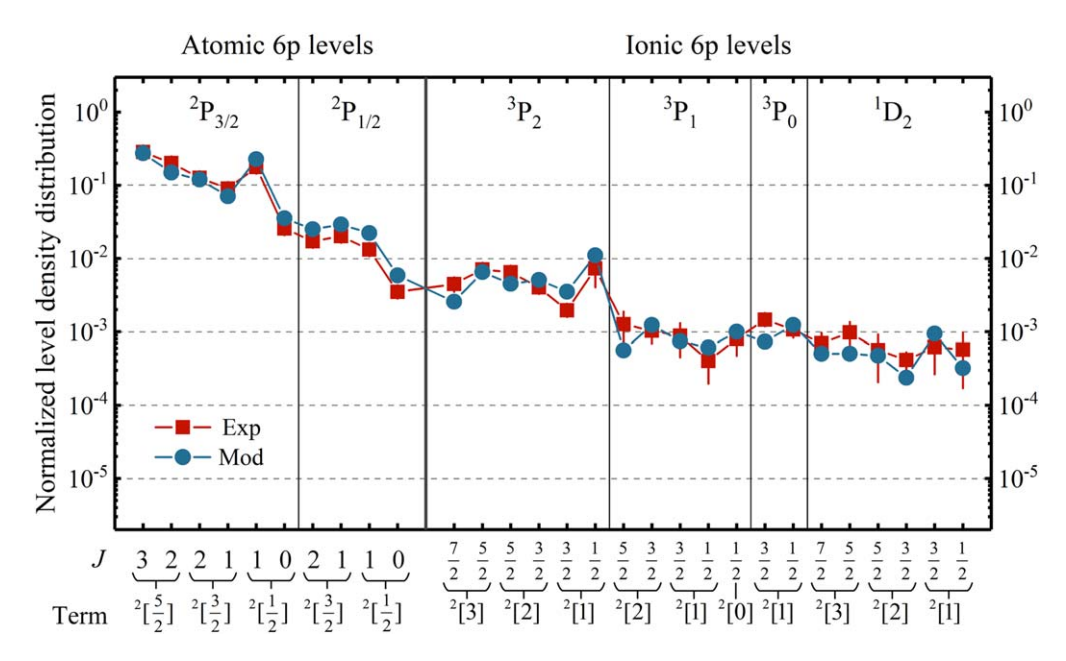


Figure 7. Normalized 6p density in the plume region (600 mm) of thruster P140.

In figure 7 the level density distribution in the plume region (HET-P140, 600 mm from exit) is changed again in comparison with the above ones. For example, the density ratio of $(^3P_2)$ $^2[1]^{\circ}_{1/2}$ to $(^3P_2)$ $^2[1]^{\circ}_{3/2}$ in figure 7 is higher than that in figure 6 by a factor \sim 5.

In figures 4–7 we use a log-scale considering the large difference between the level densities, but the uncertainties for some levels and the ratio between the calculated and measured densities are not obvious in this case. As a supplement, tables 8–9 collect these data from the above figures. In table 8 $n^{\rm Exp}$ and $n^{\rm Mod}$ refer to the densities from experiment and model, while $\Delta n^{\rm Exp}$ denotes the experimental uncertainty in level density. Four causes are considered to estimate

 $\Delta n^{\rm Exp}$, that is, (a) the noise in the optical measurement (significant for some groups e.g. $^{1}{\rm D}_{2}$ emitting weak lines but ignorable for some others, e.g. the $^{2}{\rm P}_{3/2}$ emitting strong lines), (b) the uncertainty in the Einstein coefficient data, (c) the uncertainty of spectral response of the optical system, and (d) a possible inaccuracy in the escape factor caused by the plasma non-uniformity [73]. For example, in the near-anoderegion, a total uncertainty of \sim 20% is estimated for the level $(^{2}{\rm P}^{\circ}_{3/2})^{\ 2}[5/2]_{3}$ by considering 10% due to (d) and another 10% due to (c) and (b). The uncertainty source (a) is not important for this level, but it is much more significant e.g. for the level $(^{2}{\rm P}^{\circ}_{1/2})^{\ 2}[1/2]_{0}$, leading to a total uncertainty of \sim 50%.

Table 8. Ratio between the measured and calculated densities of Xe(6p) and the total uncertainty.

E	nergy lev	el		$n^{\mathrm{Exp}}/n^{\mathrm{Mod}}(\Delta n^{\mathrm{Exp}}/n^{\mathrm{Exp}} \times 100\%)$					
Configuration	Term	J	NIST No	Near-anode (-13 mm)	Ionization (-8 mm)	Acceleration (-3 mm)	Plume (600 mm)		
$5p^5(^2P^{\circ}_{3/2}) 6p$	² [5/2]	3	8	1.22 (20%)	1.09 (20%)	1.13 (21%)	0.97 (15%)		
$5p^5(^2P^{\circ}_{3/2}) 6p$	$^{2}[5/2]$	2	7	1.09 (14%)	1.17 (21%)	1.17 (26%)	1.37 (17%)		
$5p^5(^2P^{\circ}_{3/2}) 6p$	$^{2}[3/2]$	2	10	1.00 (16%)	1.02 (20%)	1.07 (21%)	1.03 (15%)		
$5p^5(^2P^{\circ}_{3/2}) 6p$	$^{2}[3/2]$	1	9	1.09 (12%)	1.27(11%)	1.11(11%)	0.71(10%)		
$5p^5(^2P^{\circ}_{3/2}) 6p$	$^{2}[1/2]$	1	6	0.83 (21%)	0.83(21%)	0.90(23%)	1.33 (31%)		
$5p^5(^2P^{\circ}_{3/2}) 6p$	$^{2}[1/2]$	0	13	0.70 (43%)	0.83 (12%)	0.56 (12%)	1.12 (12%)		
$5p^5(^2P^{\circ}_{1/2}) 6p$	$^{2}[3/2]$	2	34	0.54 (16%)	0.62 (11%)	0.91 (14%)	1.26 (10%)		
$5p^5(^2P^{\circ}_{1/2}) 6p$	$^{2}[3/2]$	1	24	0.61 (20%)	0.81 (12%)	0.87 (30%)	0.79 (18%)		
$5p^5(^2P^{\circ}_{1/2}) 6p$	$^{2}[1/2]$	1	36	0.56 (20%)	0.66 (14%)	0.70 (42%)	0.73 (15%)		
$5p^5(^2P^{\circ}_{1/2}) 6p$	$^{2}[1/2]$	0	38	0.39 (50%)	0.64 (12%)	1.08 (18%)	1.30 (10%)		

Table 9. Ratio between the measured and calculated densities of $Xe^+(6p)$ and the total uncertainty.

]	Energy le	evel		$n^{\mathrm{Exp}}/n^{\mathrm{Mod}}(\Delta n^{\mathrm{Exp}}/n^{\mathrm{Exp}} \times 100\%)$					
Configuration	Term	J	NIST No	Near-anode (-13 mm)	Ionization (-8 mm)	Acceleration (-3 mm)	Plume (600 mm)		
$5p^4(^3P_2)6p$	² [3]°	7/2	31	1.76 (30%)	1.54 (15%)	1.40 (18%)	2.51 (22%)		
$5p^4(^3P_2)6p$	² [3]°	5/2	29	1.14 (16%)	0.85 (11%)	0.70 (11%)	1.05 (10%)		
$5p^4(^3P_2)6p$	² [2]°	5/2	26	1.24 (20%)	1.24 (11%)	0.82 (12%)	1.40 (12%)		
$5p^4(^3P_2)6p$	² [2]°	3/2	25	0.47 (79%)	0.59 (22%)	0.49 (20%)	0.80 (11%)		
$5p^4(^3P_2)6p$	² [1]°	3/2	35	_	1.11 (24%)	1.46 (27%)	0.57 (20%)		
$5p^4(^3P_2)6p$	² [1]°	1/2	30	_	0.64 (38%)	0.61 (58%)	0.71 (42%)		
$5p^4(^3P_1)6p$	² [2]°	5/2	41	_	1.79 (48%)	1.16 (57%)	2.46 (47%)		
$5p^4(^3P_1)6p$	² [2]°	3/2	42	_	0.97 (32%)	1.13 (26%)	0.98 (32%)		
$5p^4(^3P_1)6p$	² [1]°	3/2	44	_	0.86 (69%)	0.98 (42%)	1.21 (47%)		
$5p^4(^3P_1)6p$	² [1]°	1/2	46	_	1.22 (61%)	0.66 (63%)	0.63 (50%)		
$5p^4(^3P_1)6p$	² [0]°	1/2	39	_	0.75 (29%)	0.80 (30%)	0.93 (35%)		
$5p^4(^3P_0)6p$	² [1]°	3/2	40	_	1.14 (57%)	1.45 (46%)	1.95 (16%)		
$5p^4(^3P_0)6p$	² [1]°	1/2	37	_	0.63 (58%)	0.87 (55%)	0.56 (30%)		
$5p^4(^1D_2)6p$	² [3]°	7/2	52	_	3.73 (54%)	3.03 (62%)	1.42 (36%)		
$5p^4(^1D_2)6p$	² [3]°	5/2	49	_	2.56 (43%)	2.18 (33%)	2.03 (38%)		
$5p^4(^1D_2)6p$	² [2]°	5/2	54	_	1.74 (54%)	1.14 (57%)	1.48 (60%)		
$5p^4(^1D_2)6p$	² [2]°	3/2	53	_	2.13 (35%)	1.17 (29%)	2.45 (26%)		
$5p^4(^1D_2)6p$	² [1]°	3/2	51	_	1.01 (59%)	1.39 (66%)	0.80 (55%)		
$5p^4(^1D_2)6p$	² [1]°	1/2	56	_	2.58 (58%)	4.64 (57%)	1.86 (67%)		

Note that, the uncertainties in the Einstein coefficients can be estimated by comparing the calculated and measured data (for example, see [26]); one can also examine the total uncertainty in the emission line-ratios due to the sources (b), (c), and (d) by comparing the measured branching ratios with those calculated from our CR model (see data in figure 2).

4.2. Kinetics of the 6p levels

Figures 8–11 show the dominant kinetic processes of four selected 6*p* levels in the CR model. The straight solid lines are for the electron-impact processes, the inflexion solid lines for the radiation processes, and the dashed lines for some other special processes. The number on each line is the percentage contribution of this process to production or loss, that is, the total production and loss rates are normalized to 100 here.

The discharge condition of the near-anode-region is similar to some inductive plasmas at low pressures, for which the CR model of Xe(6p) has been studied [62, 63]. Thus it is understandable that the self-absorption process by atomic metastable level plays an important role in figure 8(a). The main difference between the kinetics of atomic (²P°_{3/2}) $^{2}[5/2]_{3}$ and $^{2}P^{\circ}_{3/2})$ $^{2}[1/2]_{0}$ levels lies in the production channels. Level $({}^{2}P^{\circ}_{3/2})^{-2}[5/2]_{3}$ is mainly produced by electron-impact excitation out of Xe(6s); contributions of the excitation from the ground state Xe(gs) and the decay from the high-lying levels Xe(hl) are comparable (here Xe(hl) includes the 7s, 7p, and 6d levels). However, Level (${}^{2}P^{\circ}_{3/2}$) $^{2}[1/2]_{0}$ is mainly produced by ground-state excitation, while the other processes are much weaker. Similar kinetic behaviors are also found in Ar and Kr discharges, which are well understood from studying CR models in the past [62, 63].

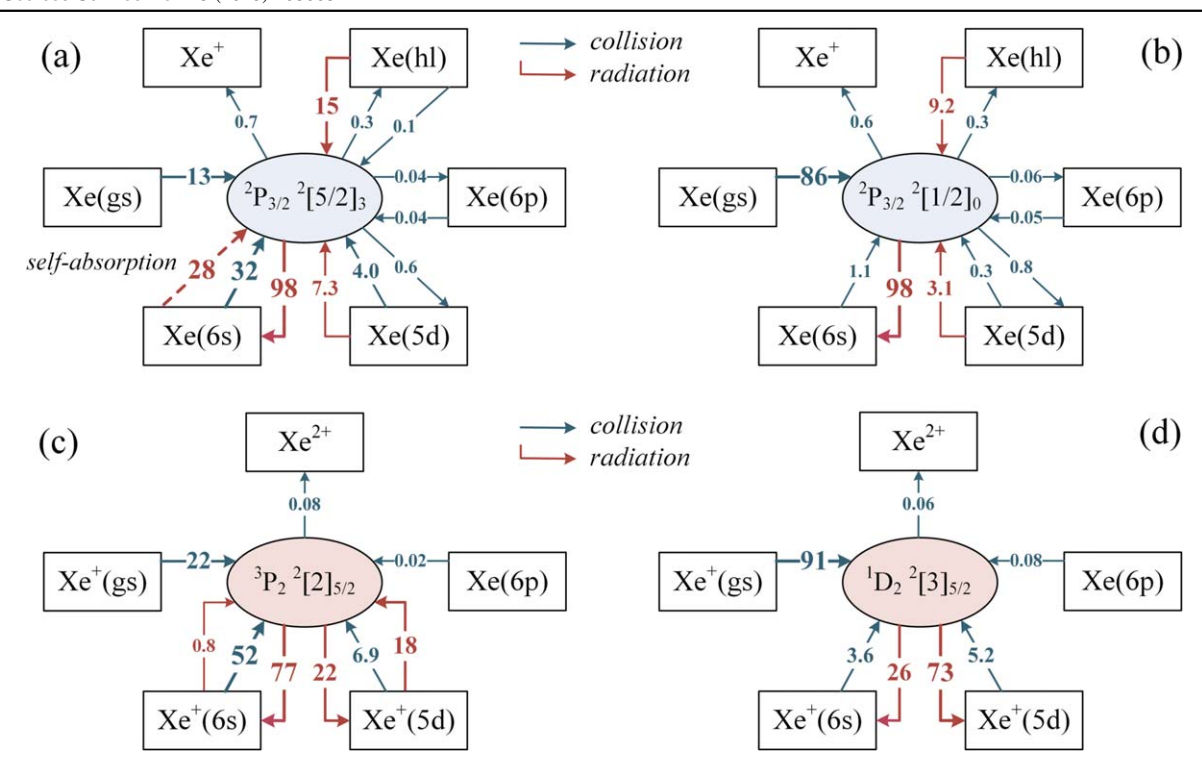


Figure 8. Diagram of kinetic processes of two Xe(6p) levels (figures (a) and (b)) and two $Xe^+(6p)$ levels (figures (c) and (d)) in the near-anode-region (-13 mm). The straight solid line, inflexion solid line, and dashed line denote the electron-impact, radiation, and other processes. The number on the line is the percentage contribution of the process to production or depopulation.

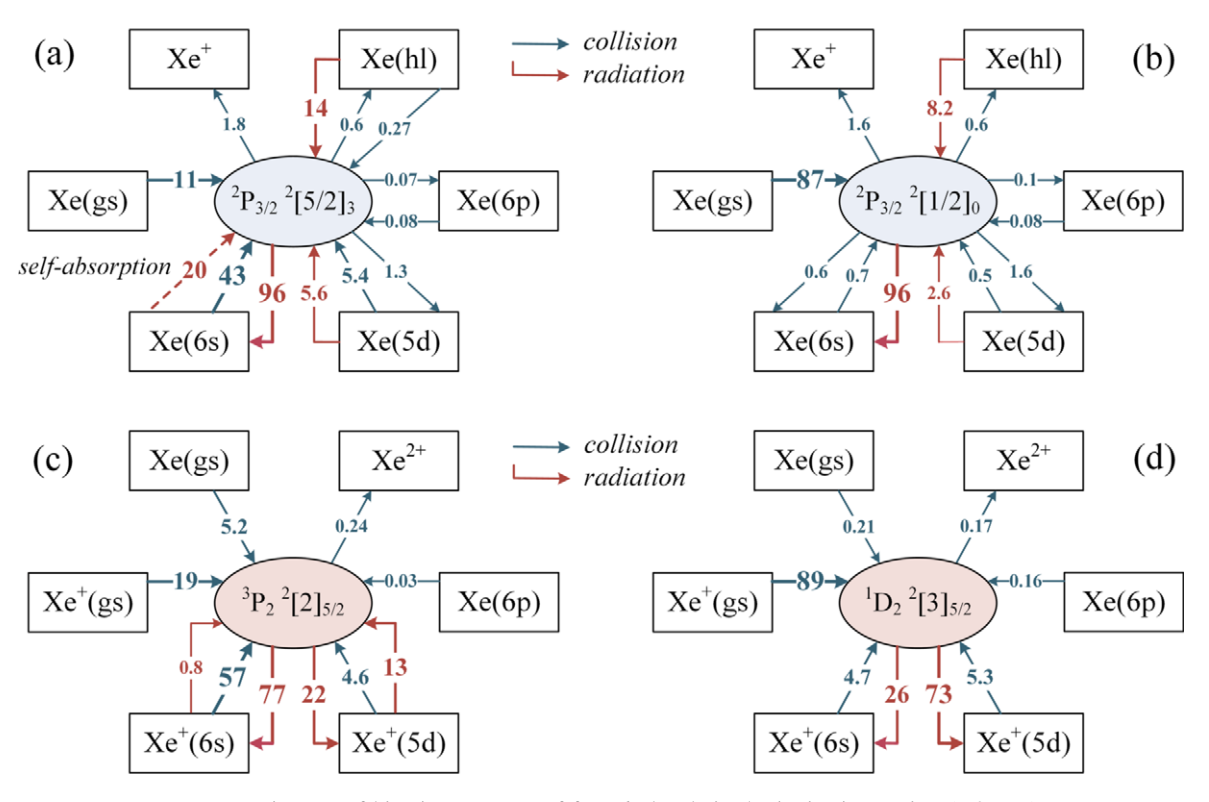


Figure 9. Diagram of kinetic processes of four 6p levels in the ionization region (-8 mm).

Unlike the atomic levels, the kinetics of the excited raregas ions in non-equilibrium plasmas has not been studied in detail yet. For the first step, we investigate two typical levels ${}^{3}P_{2}$) ${}^{2}[2]^{\circ}_{5/2}$ and ${}^{1}D_{2}$) ${}^{2}[3]^{\circ}_{5/2}$ of $Xe^{+}(6p)$. In figure 8 the

main difference in the kinetics of these levels is the production mechanism. In figure 9 the contribution of self-absorption becomes lower; this kind of variation in escape factor is valuable for OES diagnostics of neutral species [88, 89].

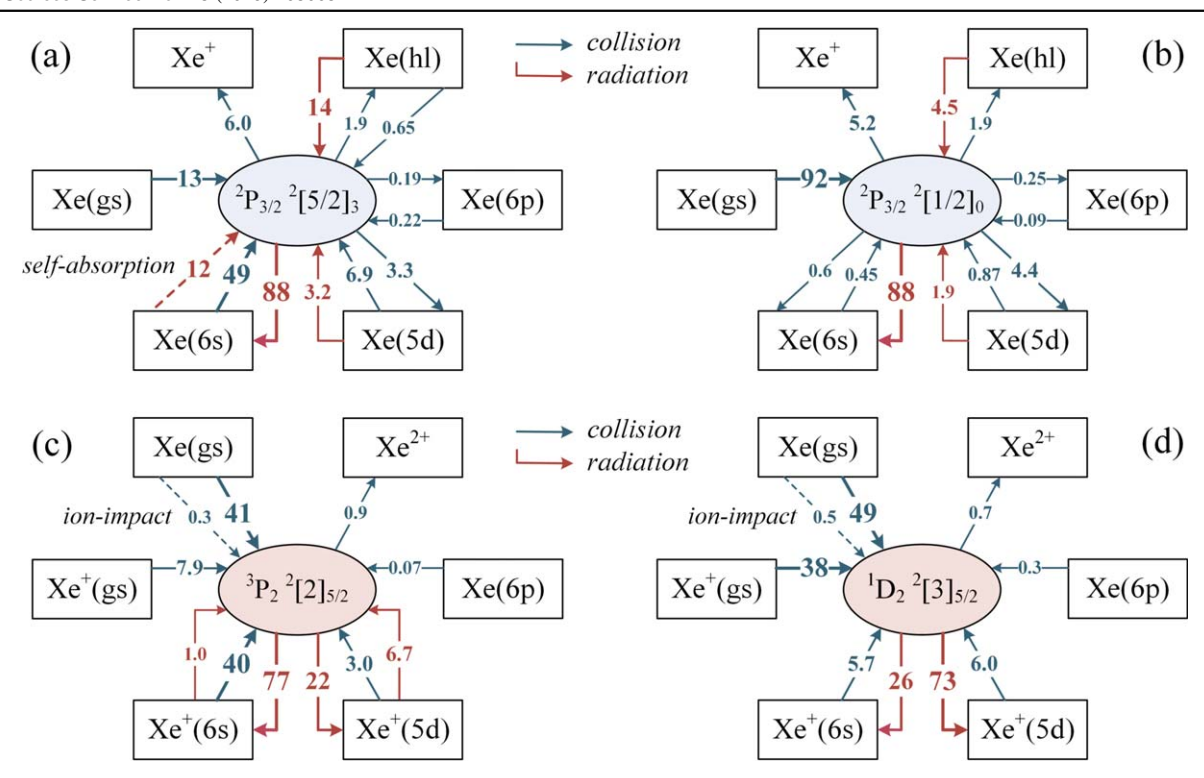


Figure 10. Diagram of kinetic processes of four 6p levels in the acceleration region (-3 mm).

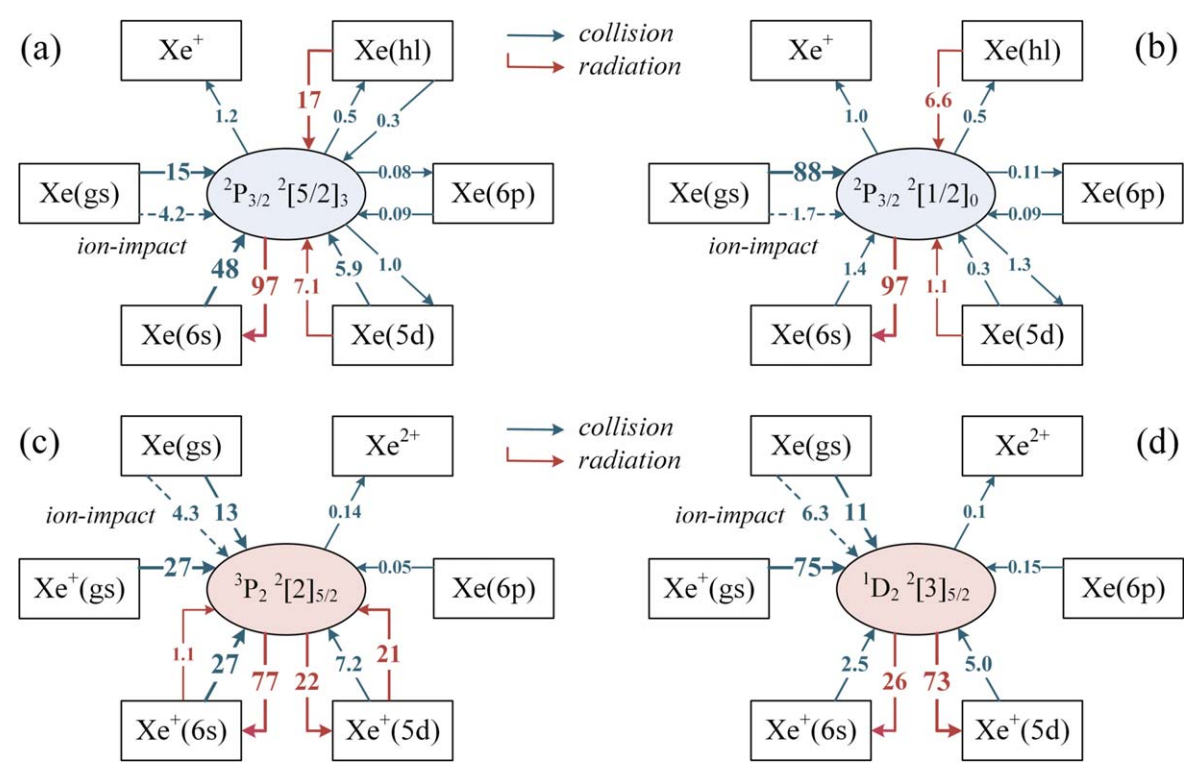


Figure 11. Diagram of kinetic processes of four 6p levels in the plume region (600 mm).

In figure 10, the electron-impact ionization-excitation process from Xe(gs) is important for the production of $Xe^+(6p)$ levels. The self-absorption becomes weaker, while the contribution of electron-impact ionization processes is around 5% for the 6p levels, which is the maximum value for

this kind of processes among the different regions. In the plume region (figure 11), the ionization-excitation process is less important, owing to a relatively low electron temperature, but its contribution is still higher than those in the near-anode-and ionization-region with Bugrova EEDF because of the

Table 10. Ratios of production rates of Xe(6p) from three groups of processes: (a) ground-state excitation by electrons and radiative decay from high-lying levels, (b) excitation or de-excitation by electrons from metastable or excited levels, and (c) self-absorption. The ratio of (c) is omitted when very small.

E	nergy lev	el		Group (a): Group (b): Group (c)					
Configuration	Term	J	NIST No	Near-anode (-13 mm)	Ionization (-8 mm)	Acceleration (-3 mm)	Plume (600 mm)		
$5p^5(^2P^{\circ}_{3/2}) 6p$	² [5/2]	3	8	34: 37: 29	31: 49: 20	30: 57: 13	37: 59		
$5p^5(^2P^{\circ}_{3/2}) 6p$	$^{2}[5/2]$	2	7	77: 21: 2	73: 26: 1	70: 28: 1	66: 27		
$5p^5(^2P^{\circ}_{3/2}) 6p$	$^{2}[3/2]$	2	10	53: 36: 11	48: 45: 7	45: 51: 4	48: 48		
$5p^5(^2P^{\circ}_{3/2}) 6p$	$^{2}[3/2]$	1	9	88: 12	84: 16	79: 20	73: 17		
$5p^5(^2P^{\circ}_{3/2}) 6p$	$^{2}[1/2]$	1	6	50: 39: 11	46: 47: 7	42: 53: 4	44: 52		
$5p^5(^2P^{\circ}_{3/2}) 6p$	$^{2}[1/2]$	0	13	98: 2	99: 1	98: 2	96: 2		
$5p^5(^2P^{\circ}_{1/2}) 6p$	$^{2}[3/2]$	2	34	75: 25	71: 29	60: 40	68: 30		
$5p^5(^2P^{\circ}_{1/2}) 6p$	$^{2}[3/2]$	1	24	75: 25	68: 32	54: 45	64: 32		
$5p^5(^2P^{\circ}_{1/2}) 6p$	$^{2}[1/2]$	1	36	78: 22	72: 28	64: 36	68: 29		
$5p^5(^2P^{\circ}_{1/2}) 6p$	$^{2}[1/2]$	0	38	29: 71	24: 76	17: 83	23: 77		

Table 11. Ratios of production rates of $Xe^+(6p)$ from three groups of processes: (a) electron excitation from two ionic ground states $(5s^25p^5)$ states with J=3/2 and 1/2) and radiative decay from higher levels, (b) electron-impact excitation or de-excitation from metastable and excited levels, and (c) electron-impact ionization-excitation. The ratio of (c) is omitted when small.

I	Energy le	evel		Group (a): Group (b): Group (c)					
Configuration	Term	J	NIST No	Near-anode (-13 mm)	Ionization (-8 mm)	Acceleration (-3 mm)	Plume (600 mm)		
$5p^4(^3P_2)6p$	² [3]°	7/2	31	92: 8	91: 7: 2	74: 8: 17	85: 9: 3		
$5p^4(^3P_2)6p$	² [3]°	5/2	29	89: 11	80: 15: 5	37: 23: 40	71: 14: 13		
$5p^4(^3P_2)6p$	² [2]°	5/2	26	39: 61	31: 64: 5	15: 44: 41	32: 57: 8		
$5p^4(^3P_2)6p$	² [2]°	3/2	25	53: 47	42: 51: 7	20: 34: 46	42: 44: 11		
$5p^4(^3P_2)6p$	² [1]°	3/2	35	87: 13	83: 15: 2	57: 21: 22	76: 15: 6		
$5p^4(^3P_2)6p$	² [1]°	1/2	30	36: 64	30: 66: 4	14: 49: 37	28: 58: 13		
$5p^4(^3P_1)6p$	² [2]°	5/2	41	84: 16	73: 24: 3	20: 32: 47	60: 21: 12		
$5p^4(^3P_1)6p$	² [2]°	3/2	42	88: 12	84: 15: 1	42: 24: 34	72: 17: 7		
$5p^4(^3P_1)6p$	² [1]°	3/2	44	91: 9	85: 13: 2	33: 23: 44	70: 14: 10		
$5p^4(^3P_1)6p$	² [1]°	1/2	46	97: 3	95: 3: 2	36: 4: 60	75: 4: 14		
$5p^4(^3P_1)6p$	² [0]°	1/2	39	92: 8	85: 14: 1	35: 26: 39	69: 12: 16		
$5p^4(^3P_0)6p$	² [1]°	3/2	40	88: 12	82: 17: 1	34: 26: 40	66: 16: 15		
$5p^4(^3P_0)6p$	² [1]°	1/2	37	96: 4	94: 5: 1	54: 10: 36	82: 6: 10		
$5p^4(^1D_2)6p$	² [3]°	7/2	52	77: 23	73: 27	40: 37: 23	67: 29: 4		
$5p^4(^1D_2)6p$	² [3]°	5/2	49	91: 9	90: 10	39: 12: 49	72: 11: 11		
$5p^4(^1D_2)6p$	² [2]°	5/2	54	88: 12	85: 15	25: 15: 60	60: 13: 24		
$5p^4(^1D_2)6p$	² [2]°	3/2	53	90: 10	88: 12	26: 8: 66	54: 10: 32		
$5p^4(^1D_2)6p$	² [1]°	3/2	51	94: 6	93: 7	75: 11: 14	88: 9: 3		
$5p^4(^1D_2)6p$	² [1]°	1/2	56	78: 22	77: 23	48: 20: 32	67: 21: 11		

high-energy tail of Maxwellian form. In addition, the ion-impact excitation plays a role for production of 6p levels here, with a typical contribution $\sim 5\%$.

To summarize the kinetic processes in the above figures, it is found that the radiation decay is always the dominant depopulation mechanism for the 6p levels. The other processes e.g. the electron-impact ionization, excitation, and deexcitation contribute altogether at most $\sim 10\%$ for the loss of Xe(6p) levels when both the electron temperature and density are high (figure 10). But even under such a condition, the contribution of radiation is still $\sim 99\%$ for the depopulation of $Xe^+(6p)$, owing to the much higher radiation decay frequencies of $Xe^+(6p)$ than those of Xe(6p). The self-absorption process by metastable atoms is strong in the near-anoderegion, weak in the acceleration-region, and negligible in the

plume-region, which shows a sensitive dependence on the atomic density. Absorption by the ionic metastable levels, however, is not observed in the current experiment.

In view of the optical line-ratio method, we collect the ratios of production rates of different processes in table 10. For the atomic 6p levels, the production processes are divided into three groups: (a) the ground-state excitation by electrons and radiative decay from the high-lying levels, (b) the electron-impact excitation or de-excitation from the metastable and excited levels, and (c) the self-absorption. Generally speaking, the processes in group (a) are sensitive to the density of high-energy electrons, group (b) is sensitive to low-energy electrons, and group (c) is sensitive to the metastable density. For the ionic 6p levels, a similar table 11 is given. Here group (c) is replaced by the electron-impact

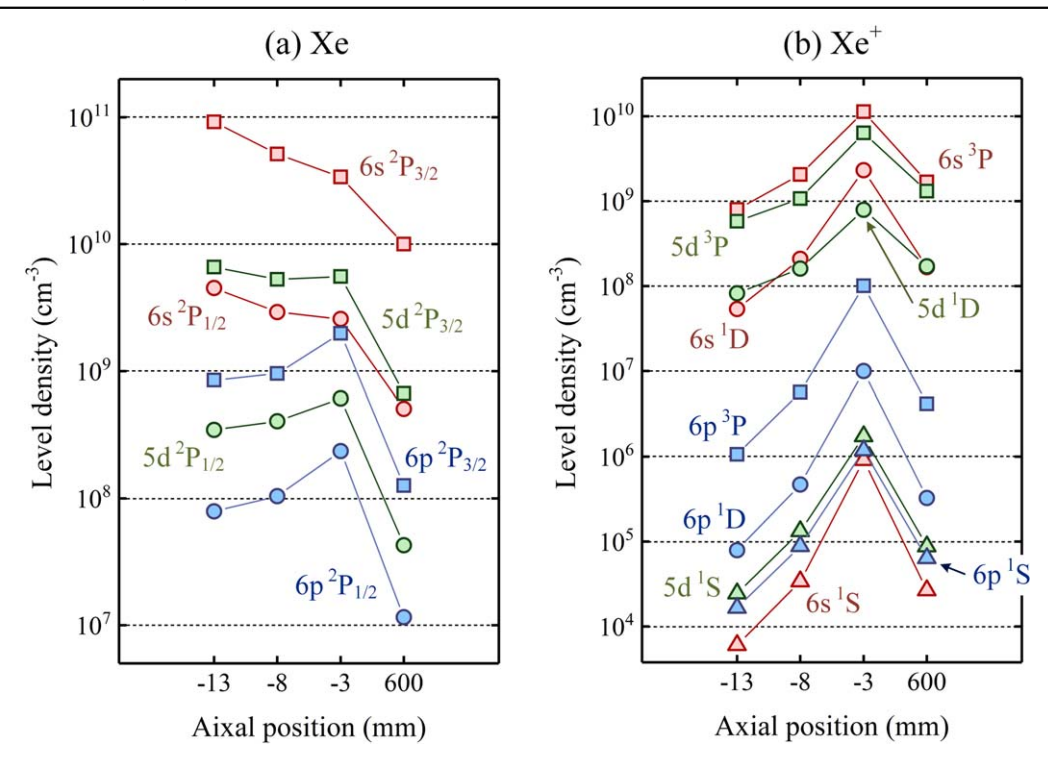


Figure 12. Calculated densities of 6s, 6p, and 5d levels with different cores in two Hall thrusters (-13, -8, and -3 mm of HET-P70) and 600 mm of HET-P140.

ionization-excitation process that depends on the very high energy tail of EEDF. Tables 10 and 11 are useful when one studies how to select emission lines for diagnostic purpose. As for the percentage contribution of ion-impact excitations, it can be directly obtained by subtracting the numbers of groups (a)–(c) in these tables from 100.

4.3. Densities of 6s and 5d levels

Although a comprehensive experimental study of the 6s and 5d density distributions cannot be performed here, the modelling results are still valuable for understanding some characteristics. Figure 12 shows the density variation of several groups of excited species with different cores at four positions of Hall thrusters. Firstly, we find that the peak density of the two groups of Xe(6s) occurs in the near-anode-region, which is reasonable considering the relatively high density of Xe atoms here. For the group $Xe(5d^2P_{3/2})$ the density profile is relatively flat in the discharge channel and for the other groups the peak density is in the acceleration region where the electron temperature is high. Secondly, we find the density of Xe(5d) group can be higher than that of Xe(6p) group with the same core, being opposite to their energy order. The group densities of Xe⁺(6s) and Xe⁺(5d) with ³P and ¹D cores are much higher than that of $Xe^+(6p)$. From a detailed analysis, we find there are four important metastable levels and eight important quasi-metastable levels in total under the condition of this work, including $(^3P_2)$ $^2[4]_{9/2}$, $(^3P_2)$ $^2[4]_{7/2}$, $(^3P_2)$ $^2[3]_{7/2}$, $(^3P_2)$ $^2[2]_{5/2}$, $(^3P_2)$ $^2[2]_{3/2}$, $(^3P_1)$ $^2[3]_{7/2}$, $(^1D_2)$ $^2[4]_{9/2}$, and $({}^{1}D_{2})^{2}[4]_{7/2}$ of $Xe^{+}(5d)$ and $({}^{3}P_{2})^{2}[2]_{5/2}$, $({}^{3}P_{2})^{2}[2]_{3/2}$, $({}^{3}P_{1})^{2}[1]_{3/2}$, and $({}^{1}D_{2})^{2}[2]_{5/2}$ of Xe⁺(6s). Their densities are high in comparison with the other excited states of Xe^+ and play a dominant role in the production of $Xe^+(6p)$.

In general, one can find that the level densities depend on the core of the levels in figure 12, which can be understood as a significant evidence of j–j coupling.

5. Discussion and open questions

Two kinds of EEDFs are assumed in the present model, Maxwellian and Bugrova distributions, as found outside and inside of the discharge channel of Hall thrusters, respectively [23, 68]. The Bugrova form is caused owing to the depletion of high-energy tail of EEDF by the electron-wall interactions. This effect is significant for the region near the anode, but weak for the region near the channel exit. Actually, concerning the electron kinetics in the magnetic field of Hall thrusters, an anisotropic EEDF is more likely. The distribution of the electron velocity components parallel to the magnetic lines of force may be significantly different from that of the perpendicular component. This provides us an opportunity of investigating Hall thrusters by plasma polarization spectroscopy [90, 91], which is an attractive topic and planned for a future work with new setup.

6. Conclusion

In the present work, we propose a CR model focusing on the kinetics of 6s, 6p, and 5d excited levels of both the neutral Xe atom and the Xe^+ ion for studying EP devices. Experimental

examination of the model is performed by using 1 and 5 kW magnetic focusing Hall thrusters. The calculated and measured results are in general agreement, which demonstrates that the fundamental data of cross sections and Einstein coefficients provided by a fully relativistic Dirac *B*-spline *R*-matrix approach in our previous work are generally accurate. Based on these results, further development of the CR model and its possible application to the OES method are discussed and will be studied in detail in the following paper of this series of works.

Acknowledgments

The authors would like to express their gratitude to Mr Shi-Lin Yan, Dr Hong Li, Ms Xing-Yu Liu, and Mr You Wu for their help in the experiment and to Professor Wonho Choe, Dr Zhong-Xi Ning, and Dr Hui Liu for inspiring discussions. This work is financially supported by the National Natural Science Foundation of China under grant Nos. 11775063, 51736003, and 11404081 and a research project under grant No. LabASP-2017–05. And by the United States National Science Foundation under grant Nos. PHY-1520970 (OZ and KB) as well as No. PHY-1403245 and No. PHY-1803844 (KB). The DBSR calculations were performed on STAM-PEDE II at the Texas Advanced Computing Center. They were made possible through the XSEDE allocation No. PHY-090031.

Appendix

A group of Excel documents is provided as supplemental material. These files contain the electron-impact rate coefficients from the ground, metastable, and quasi-metastable states and the Einstein coefficients. The data can be used to build a CR model for EP devices. A full set of rate coefficient data will also be given online through the LXCat program (https://nl.lxcat.net/).

ORCID iDs

Xi-Ming Zhu https://orcid.org/0000-0002-6501-0096 Yan-Fei Wang https://orcid.org/0000-0002-9226-8279 Klaus Bartschat https://orcid.org/0000-0001-6215-5014 Tsanko Vaskov Tsankov https://orcid.org/0000-0002-7937-486X

Uwe Czarnetzki https://orcid.org/0000-0002-5823-1501

References

- Mazouffre S 2016 Electric propulsion for satellites and spacecraft: established technologies and novel approaches *Plasma Sources Sci. Technol.* 25 033002
- [2] Sutton G P and Biblarz O 2010 Rocket Propulsion Elements (New York: Wiley)

- [3] Adamovich I et al 2017 The 2017 plasma roadmap: low temperature plasma science and technology J. Phys. D: Appl. Phys. 50 323001
- [4] Romadanov I, Raitses Y and Smolyakov A I 2018 Hall thruster operation with externally driven breathing mode oscillations *Plasma Sources Sci. Technol.* 27 094006
- [5] Zolotukhin D B and Keidar M 2018 Optimization of discharge triggering in microcathode vacuum arc thruster for CubeSats Plasma Sources Sci. Technol. 27 074001
- [6] Lev D et al 2017 The technological and commercial expansion of electric propulsion in the past 24 years Proc. 35th Int. Electr. Propuls. Conf.
- [7] Boeuf J-P 2017 Tutorial: physics and modeling of Hall thrusters J. Appl. Phys. 121 011101
- [8] Liu H et al 2015 Fluid simulation of a cusped field thruster Contrib. Plasma Phys. 55 545
- [9] Cichocki F et al 2017 Hybrid 3D model for the interaction of plasma thruster plumes with nearby objects Plasma Sources Sci. Technol. 26 125008
- [10] Liu H et al 2015 2D modeling of orificed hollow cathodes of stationary plasma thrusters SPT-100 IEEE Trans. Plasma Sci. 43 4024
- [11] Croes V et al 2017 2D particle-in-cell simulations of the electron drift instability and associated anomalous electron transport in Hall-effect thrusters Plasma Sources Sci. Technol. 26 034001
- [12] Yu D et al 2017 Confinement effect of cylindrical-separatrixtype magnetic field on the plume of magnetic focusing type Hall thruster Plasma Sources Sci. Technol. 26 04LT02
- [13] Wei L Q et al 2018 A photographic method for in-orbit measurement of electron temperature distribution in the plume of Hall thrusters Plasma Sources Sci. Technol. 27 084002
- [14] Williams G J Jr and Kamhawi H 2015 Optical characterization of component wear and near-field plasma of the HERMeS thruster 62nd Joint Army-Navy-NASA-Air Force Meeting
- [15] Hargus W A and Charles C S 2010 Near-plume laser-induced fluorescence velocity measurements of a medium power Hall thruster J. Propul. Power 26 135
- [16] Mazouffre S 2013 Laser-induced fluorescence diagnostics of the cross-field discharge of Hall thrusters *Plasma Sources Sci. Technol.* 22 013001
- [17] Young C V et al 2018 Time-resolved laser-induced fluorescence diagnostics for electric propulsion and their application to breathing mode dynamics *Plasma Sources* Sci. Technol. 27 094004
- [18] Ellison C L, Raitses Y and Fisch N J 2012 Cross-field electron transport induced by a rotating spoke in a cylindrical Hall thruster *Phys. Plasmas* 19 013503
- [19] Levchenko I et al 2018 Recent progress and perspectives of space electric propulsion systems based on smart nanomaterials Nat. Commun. 9 879
- [20] Karabadzhak G F, Chiu Y and Dressler R A 2006 Passive optical diagnostic of Xe propelled Hall thrusters. II. Collisional-radiative model J. Appl. Phys. 99 113305
- [21] Chiu Y et al 2006 Passive optical diagnostic of Xe-propelled Hall thrusters. I. Emission cross sections J. Appl. Phys. 99 113304
- [22] Dressler R A et al 2009 Near-infrared collisional radiative model for Xe plasma electrostatic thrusters: the role of metastable atoms J. Phys. D: Appl. Phys. 42 185203
- [23] Yang J et al 2010 Diagnosing on plasma plume from xenon Hall thruster with collisional-radiative model Phys. Plasmas 17 103504
- [24] LANL 2018 Los Alamos Atomic Physics Codes (https://aphysics2.lanl.gov/tempweb/lanl/)
- [25] Yang J et al 2013 Experiment study of an electron cyclotron resonant ion source based on a tapered resonance cavity Phys. Plasmas 20 123505

- [26] Wang Y, Wang Y F, Zhu X M, Zatsarinny O and Bartschat K 2018 A xenon collisional-radiative model applicable to electric propulsion devices: I. Calculations of electronimpact cross sections for xenon ions by the Dirac B-spline R-Matrix method *Plasma Sources Sci. Technol.* 28 Accepted
- [27] Zatsarinny O and Bartschat K 2010 Benchmark calculations for near-threshold electron-impact excitation of krypton and xenon atoms J. Phys. B: At. Mol. Opt. Phys. 43 074031
- [28] NIST Atomic Spectra Database 2019 (https://nist.gov/pml/ atomic-spectra-database)
- [29] Buckman S J et al 1983 High-resolution electron impact excitation functions of metastable states of neon, argon, krypton and xenon J. Phys. B: At. Mol. Phys. 16 4219
- [30] Allan M, Zatsarinny O and Bartschat K 2006 Near-threshold absolute angle-differential cross sections for electron-impact excitation of argon and xenon *Phys. Rev.* A 74 030701
- [31] Fons J T and Lin C C 1998 Measurement of the cross sections for electron-impact excitation into the 5p⁵6p levels of xenon Phys. Rev. A 58 4603
- [32] Jung R O *et al* 2005 Electron-impact excitation cross sections from the xenon J=2 metastable level *Phys. Rev.* A **72** 022723
- [33] Jung R O *et al* 2009 Excitation into $5p^57p$ levels from the ground level and the J=2 metastable level of Xe *Phys. Rev.* A **80** 062708
- [34] Bartschat K, Tennyson J and Zatsarinny O 2017 Quantummechanical calculations of cross sections for electron collisions with atoms and molecules *Plasma Process*. *Polym.* 49 1600093
- [35] Bray I *et al* 2012 Electron- and photon-impact atomic ionisation *Phys. Rep.* **520** 135
- [36] Bartschat K et al 1996 Electron scattering by complex atoms and ions at intermediate energies J. Phys. B: At. Mol. Opt. Phys. 29 115
- [37] Bartschat K 1998 The R-matrix with pseudo-states method: theory and applications to electron scattering and photoionization *Comput. Phys. Commun.* 114 168
- [38] Berrington K A, Eissner W B and Norrington P H 1995 RMATRX1: belfast atomic R-Matrix codes Comput. Phys. Commun. 92 290
- [39] Badnell N R 2018 UK APAP Codes (http://apap-network. org/codes.html)
- [40] Zatsarinny O 2006 BSR: B-spline atomic R-matrix codes Comput. Phys. Commun. 174 273
- [41] Zatsarinny O and Bartschat K 2013 The B-spline R-matrix method for atomic processes: application to atomic structure, electron collisions, and photoionization J. Phys. B: At. Mol. Opt. Phys. 46 112001
- [42] Gupta S, Sharma L and Srivastava R 2018 Electron-impact excitation of Xe⁺ and polarization of its subsequent emissions J. Quant. Spectrosc. Radiat. Transf. 219 7
- [43] Sharma L, Srivastava R and Stauffer A D 2011 Excitation of the $5p^57p$ levels of xenon by electron impact *Eur. Phys. J.* D **62** 399
- [44] Chen Z B *et al* 2014 Electron impact excitation of xenon from the ground state and the metastable state to the 5p⁵7p levels *Chin. Phys. Lett.* **31** 033401
- [45] Sommerville J D et al 2008 Ion-collision emission excitation cross sections for Xenon electric thruster plasmas J. Propul. Power 24 880
- [46] Achenbach C et al 1984 Single ionisation of multiply charged xenon ions by electron impact J. Phys. B: At. Mol. Opt. Phys. 17 1405
- [47] Mathur D and Badrinathan C 1987 Ionization of xenon by electrons: partial cross sections for single, double, and triple ionization *Phys. Rev.* A 35 1033
- [48] Deutsch H et al 2004 Calculated cross sections for the electronimpact ionization of excited argon atoms using the DM formalism Int. J. Mass Spectrom. 233 39

- [49] Kimura M and Watanabe T 1971 Charge transfer cross sections for Kr⁺-Kr and for Xe⁺-Xe and the effects of the initial J-States in the ions J. Phys. Soc. Japan. 31 1600
- [50] Sakabe S and Izawa Y 1991 Cross sections for resonant charge transfer between atoms and their positive ions: collision velocity ≤1 au At. Data Nucl. Data 49 257
- [51] Miller J S et al 2002 Xenon charge exchange cross sections for electrostatic thruster models J. Appl. Phys. 91 984
- [52] Gigosos M A et al 1994 Experimental Stark widths and shifts and transition probabilities of several Xe II lines Phys. Rev. E 49 1575
- [53] Zielińska S, Bratasz Ł and Dzierżęga K 2002 Absolute transition rates for transitions from $5p^4(^3P)6p^4P^{\circ}_{5/2}, ^4P^{\circ}_{3/2}, ^4D^{\circ}_{7/2}$ and $^2D^{\circ}_{5/2}$ levels of Xe II *Phys. Scr.* **66** 454
- [54] Di Rocco H O, Iriarte D I and Pomarico J A 2000 Lifetimes and transition probabilities of Xe II: experimental measurements and theoretical calculations *Eur. Phys. J.* D 10 19
- [55] Zatsarinny O and Bartschat K 2009 B-spline calculations of oscillator strengths in noble gases *Phys. Scr.* T134 014020
- [56] Kolts J H and Setser D W 1978 Decay rates of Ar(4s, 3P₂), Ar(4s', 3P₀), Kr(5s, 3P₂), and Xe(6s, 3P₂) atoms in argon J. Chem. Phys. 68 4848
- [57] Alekseev V A and Setser D W 1999 Generation and kinetics studies of Xe(5d[3/2]₁) resonance states atoms *J. Chem. Phys.* 103 8396
- [58] Zhu X M and Pu Y K 2010 A simple collisional–radiative model for low-temperature argon discharges with pressure ranging from 1 Pa to atmospheric pressure: kinetics of Paschen 1s and 2p levels J. Phys. D: Appl. Phys. 43 015204
- [59] Sobel'man I I, Vainshtein L A and Yukov E A 1995 Excitation of Atoms and Broadening of Spectral Lines (Berlin: Springer)
- [60] Liu H et al 2010 Particle-in-cell simulation of a Hall thruster J. Phys. D: Appl. Phys. 43 165202
- [61] Vlcek J 1989 A collisional-radiative model applicable to argon discharges over a wide range of conditions: I. Formulation and basic data J. Phys. D: Appl. Phys. 22 623
- [62] Zhu X M et al 2008 Determining the electron temperature and the electron density by a simple collisional–radiative model of argon and xenon in low-pressure discharges J. Phys. D: Appl. Phys. 42 025203
- [63] Priti, Gangwar R K and Srivastava R 2019 Collisionalradiative model of xenon plasma with calculated electronimpact fine structure excitation cross-sections *Plasma Sources Sci. Technol.* 28 025003
- [64] Dannenmayer K and Mazouffre S 2013 Electron flow properties in the far-field plume of a Hall thruster *Plasma Sources Sci. Technol.* 22 035004
- [65] Dannenmayer K et al 2014 The time-varying electron energy distribution function in the plume of a Hall thruster Plasma Sources Sci. Technol. 23 065001
- [66] Taccogna F 2015 Monte Carlo Collision method for low temperature plasma simulation J. Plasma Phys. 81 1
- [67] Bugrova A I *et al* 1982 Dynamics of the electron energy distribution function in a plasma acceleration with extended acceleration zone *High Temp.* **19** 822
- [68] Bugrova A I, Desyatskov A V and Morozov A I 1992 Electron distribution function in a Hall accelerator Sov. J. Plasma Phys. 18 501–7
- [69] Wikipedia 2018 SPT-100 (https://en.wikipedia.org/wiki/ SPT-100)
- [70] Li H et al 2018 Discharge characteristics of a Kilowatt Hall effect thruster with a variable channel Vacuum 153 291
- [71] Taccogna F and Minelli P 2018 Three-dimensional particle-incell model of Hall thruster: the discharge channel *Phys. Plasmas* 25 061208

- [72] Tsankov T V and Czarnetzki U 2017 Information hidden in the velocity distribution of ions and the exact kinetic Bohm criterion *Plasma Sources Sci. Technol.* 26 055003
- [73] Zhu X M et al 2016 Escape factors for Paschen 2p–1s emission lines in low-temperature Ar, Kr, and Xe plasmas J. Phys. D: Appl. Phys. 49 225204
- [74] Lieberman M A and Lichtenberg A J 2005 Principles of Plasma Discharges and Materials Processing (New York: Wiley)
- [75] Yang T et al 2014 Hall thruster plume divergence angle assessment method based on image processing Measurement 50 74
- [76] Yu D et al 2009 Experimental and theoretical study on effects of magnetic field topology on near wall conductivity in a Hall thruster Phys. Plasmas 16 103504
- [77] Ning Z X et al 2011 Effects of ionization distribution on plasma beam focusing characteristics in Hall thrusters Appl. Phys. Lett. 99 221502
- [78] Wei L et al 2012 Effects of coupling oscillations on the electron conductivity of Hall thrusters Contrib. Plasm. Phys. 52 761
- [79] Li H, Ning Z X and Yu D 2013 Hall thruster with grooved walls J. Appl. Phys. 113 083303
- [80] Han K et al 2012 Unstable discharge phenomenon and stabilization of Hall thruster operating in self-excited mode J. Propul. Power 28 27
- [81] Ning Z X 2009 Theoretical and experimental research on plasma beam focalization in a Hall thruster using krypton propellant *PhD Thesis* Harbin Institute of Technology Harbin

- [82] Wei L *et al* 2016 Study on the peak current of power supply during a Hall thruster start-up *Vacuum* 123 126
- [83] Yu D et al 2008 Effect of electron temperature on dynamic characteristics of two-dimensional sheath in Hall thrusters Phys. Plasmas 15 104501
- [84] Liu H et al 2015 Effect of the variable cross-section channel on performance of a cusped field thruster at low power J. Phys. D: Appl. Phys. 48 375203
- [85] Li H et al 2018 Experimental and numerical investigation of a Hall thruster with a chamfered channel wall Chin. Phys. B 27 105209
- [86] Niu X et al 2018 The influence of anode position and structure on cusped field thruster Phys. Plasmas 25 040701
- [87] Ellison C L, Raitses Y and Fisch N J 2011 Fast camera imaging of Hall thruster ignition *IEEE Trans. Plasma Sci.* 39 2950
- [88] Wang Z B *et al* 2013 The influence of the spatial nonuniformity on the measurement of Ar*(1s₅) density by the self-absorption technique *J. Phys. D: Appl. Phys.* 46 475205
- [89] Zhu X M, Tsankov T V and Czarnetzki U 2015 Self-absorption method in combination with an optical probe: a possibility to determine the radial density profile of rare-gas metastables in low-temperature plasmas *Plasma Sources Sci. Technol.* 24 035023
- [90] Fujimoto T and Kazantsev S A 1997 Plasma polarization spectroscopy *Plasma Phys. Control. Fusion* 39 1267
- [91] Fujimoto T and Iwamae A 2005 Plasma polarization spectroscopy: A + M data aspects *AIP Conf. Proc.* **771** 33